Review

Strategies for Image-Guided Therapy, Surgery, and Drug Delivery Using Photoacoustic Imaging

Colman Moore[1] and Jesse V. Jokerst[1,2,3 ✉]

1. Department of NanoEngineering
2. Materials Science and Engineering Program
3. Department of Radiology, University of California, San Diego, La Jolla, CA 92093. United States.

✉ Corresponding author: Jesse V. Jokerst, jjokerst@ucsd.edu, (858) 246-0896.

Abstract

Photoacoustic imaging is a rapidly maturing imaging modality in biological research and medicine. This modality uses the photoacoustic effect ("light in, sound out") to combine the contrast and specificity of optical imaging with the high temporal resolution of ultrasound. The primary goal of image-guided therapy, and theranostics in general, is to transition from conventional medicine to precision strategies that combine diagnosis with therapy. Photoacoustic imaging is well-suited for noninvasive guidance of many therapies and applications currently being pursued in three broad areas. These include the image-guided resection of diseased tissue, monitoring of disease states, and drug delivery. In this review, we examine the progress and strategies for development of photoacoustics in these three key areas with an emphasis on the value photoacoustics has for image-guided therapy.

Key words: photoacoustic imaging, ultrasound, image-guided, therapy, surgery, drug delivery

1. Introduction

1.1. History of Photoacoustic Imaging

In the past few decades, photoacoustic imaging (PAI) has emerged as a novel imaging modality with a variety of promising applications in medicine. In contrast to traditional X-ray imaging, positron-emission tomography (PET), and computed tomography (CT), PAI is capable of revealing structural, functional, and molecular information of biological systems without ionizing radiation by integrating optical excitation with ultrasound detection. This hybrid technique relies on the photoacoustic effect—the generation of acoustic waves as light is converted to heat following optical absorption. In the body, PAI can be used to image intrinsic components of tissue such as hemoglobin and melanin, as well as extrinsic contrast agents targeted to biomarkers or specific regions of the body.

Today, PAI is being developed for a wide range of image-guided applications including the monitoring and therapy of disease states, drug delivery, and surgical guidance. A number of review articles on PAI exist in the literature. These range from emphases on contrast agents or specific applications to more general overviews [1-6]. For contrast agents, both broad surveys [7-10] and spotlights on particular types such as ratiometric probes [11], activatable probes [12], inorganic nanomaterials [13-16], photo-thermal probes [17], NIR-II probes [18, 19], and organic probes [19-23] are recommended to the reader. In addition, applications reviewed include imaging the brain [24, 25], microvasculature [26], cancer [27], and drug delivery [28]. The purpose of this review is to highlight image-guided applications of PAI, assess developments in the technology, and examine progress towards clinical translation.

Alexander Graham Bell first reported the photoacoustic (PA) effect in 1880 following his experiments on the photophone, the world's first wireless communications device [29]. He described the generation of sound waves by various materials in response to pulses of sunlight [30]. These observations

were overlooked for many years, but have since been studied extensively, and the physics of the PA effect were expounded by Rosencwaig and Gersho, of Bell Labs, for photoacoustic spectroscopy [31]. They predicted its utility for biomedical imaging because of its ability to obtain optical absorption spectra for almost all solids and semisolids, its insensitivity to light scattering, and its noninvasive nature. Not long after, a method was developed for acquiring 1D PA signal in synthetic scattering media using a single transducer element following a pulse of ionizing radiation [32]. In the 1990s, non-ionizing light was harnessed for signal propagation, and the technology was extended to 3D imaging in biological tissue, along with theoretical underpinnings of PA ultrasound reconstruction tomography [33-35] and microwave-induced acoustic tomography [36]. Since then, major developments in PAI have included photoacoustic tomography (PAT), photoacoustic computed tomography (PACT), photoacoustic microscopy (PAM), handheld imaging devices, and customized contrast agents [37]. In this review, we provide an overview of the emerging roles these PA technologies are playing in image-guided therapy, surgery, and drug delivery (Figure 1).
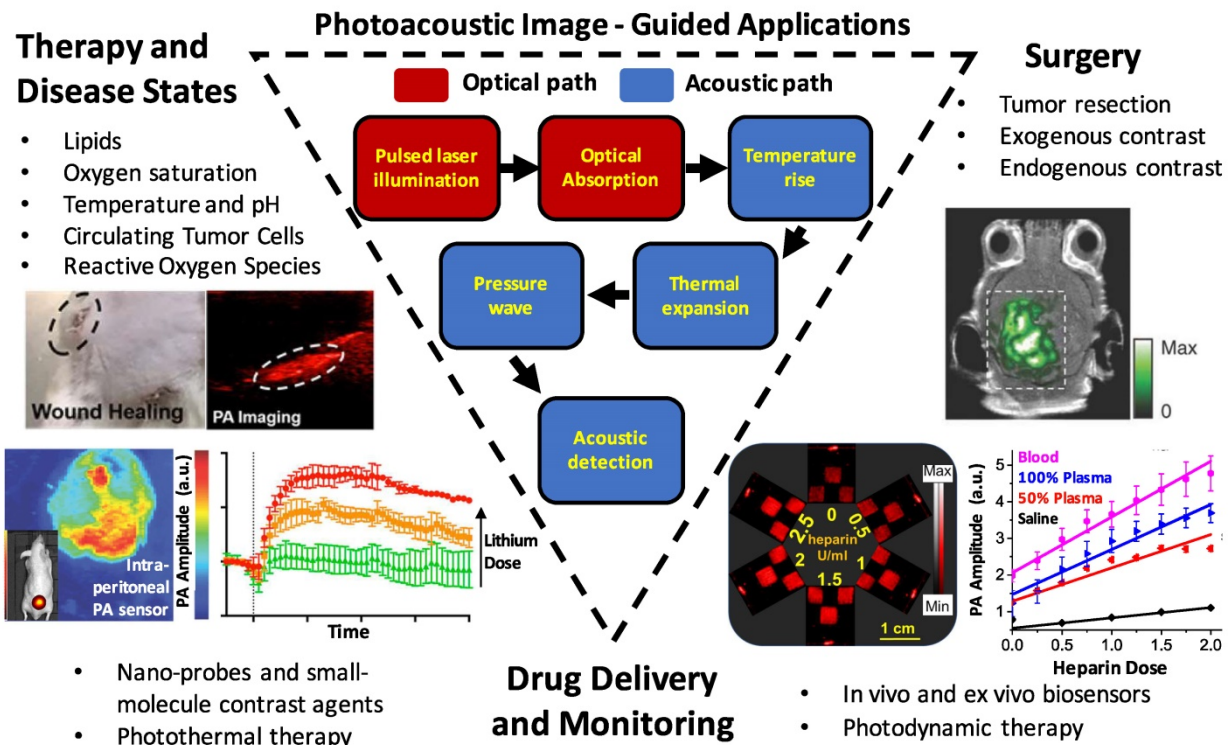
1.2. Principles of PAI

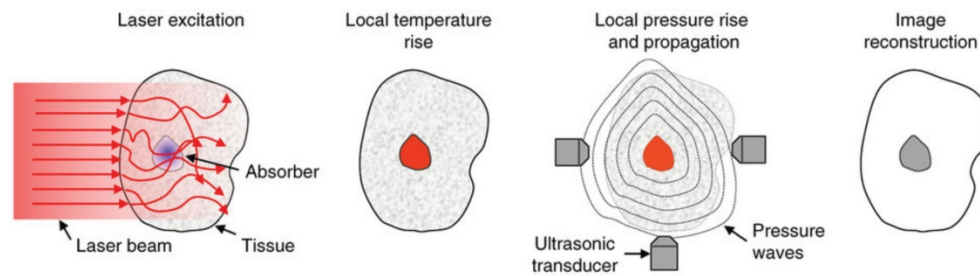PAI is a *hybrid* imaging modality because it combines the high contrast and specificity of optical imaging with the strong temporal resolution and increased penetration depth of ultrasound. PAI (sometimes called optoacoustic imaging) takes advantage of the photoacoustic effect and typically uses near-infrared (NIR) or visible light to leverage the optical window— a range of non-ionizing wavelengths that allow for deeper penetration in human tissue [38, 39]. The photoacoustic effect consists of three distinct steps in soft matter [40]:

- The target absorbs a photon.
- The target increases in temperature, inducing a local pressure increase via thermoelastic expansion.
- The pressure perturbation is propagated throughout the surrounding medium by elastic interactions.

The generation of acoustic waves requires thermal expansion to be time variant. To achieve this in PAI, a pulsed laser is used (1-100 ns), or a continuous-wave (CW) laser is intensity modulated to excite a light-absorbing target [41, 42]. Pulsed lasers are the most common because they have a better signal to noise ratio than CW lasers at constant fluence and power [43]. In addition, laser pulses are shorter than the thermal and stress confinement times of absorbers, meaning thermal diffusion and volume expansion can be neglected during illumination [4].

Figure 1. Summary schematic of the topics examined in this article: image-guided surgery (including tumor margination and resection, endogenous contrast mechanisms, and endogenous contrast agents), drug delivery and monitoring (including photothermal/photodynamic therapies, nanoparticle and molecular contrast agents, and biosensors), and monitoring therapy and disease states (including targets such as reactive oxygen species, hemodynamics/blood oxygen saturation, temperature/pH, circulating tumor cells, and lipids).

Figure 2. Schematic of the principles of PAI. Light is absorbed by a target, raising the local temperature. Thermoelastic expansion propagates pressure waves in the ultrasonic range through surrounding tissue. Ultrasound transducers detect the waves and images are constructed based on their strength and times of arrival. Adapted with permission from [5], copyright 2016 Nature Publishing Group.

Table 1. Major hardware configurations of PAI with representative performance metrics.

Technique	Full Name	Brief Description	Resolution	Imaging Depth
OR-PAM	Optical Resolution - Photoacoustic Microscopy [49, 50]	A laser is focused to a diffraction-limited spot with a microscope objective and the generated acoustic signal is focused with a concave acoustic lens to be detected by a broadband ultrasound transducer.	~0.5 - 3.0 µm	~1.2 mm
AR-PAM	Acoustic Resolution - Photoacoustic Microscopy [3]	A dark-field ring of light is focused onto tissue and a concave acoustic lens focuses the acoustic signal to a broadband ultrasound transducer.	~45 µm	~5 mm
PAT/PACT	Photoacoustic Tomography / Computed Tomography [5]	A pulsed illumination beam excites a region of interest and a linear or circular transducer array receives acoustic signal for image generation using inverse/back-projection algorithms.	0.1 - 1.0 mm	Multiple centimeters possible
PAE	Photoacoustic Endoscopy [60]	Optical excitation, acoustic transduction, and mechanical scanning components are confined to the distal tip of an endoscope.	31 - 170 µm	1 - 7 mm

In tissue, the interaction of photons with cellular structures results in elastic scattering. The molecules struck by these scattered photons undergo thermoelastic expansion generating wideband acoustic waves (ultrasonic) in the surrounding medium [44]. These waves are detectable by an array of piezoelectric transducers and images can be generated by measuring the waves' amplitudes and arrival times to reconstruct the initial photoacoustic pressure distribution. This process is represented schematically in Figure 2.

The initial amplitudes of PA waves can be determined according to Equation 1.

$$P_0 = \Gamma \eta_{th} \mu_a F \qquad (1)$$

Here, P_0 is the initial local pressure rise (PA amplitude) that initiates ultrasonic wave propagation. The PA efficiency is dictated by the Grüneisen parameter Γ (dimensionless), a thermodynamic property that scales with temperature and differs between absorbing targets, and η_{th}, the heat conversion efficiency (equivalent to the amount of nonradiative energy decay following the laser pulse, or, 1 minus the fluorescence quantum yield) [4, 28]. Because Γ is temperature dependent, PAI can be used to monitor temperature [45]. The optical absorption coefficient, μ_a (cm^{-1}), is proportional to the concentration of the chromophore target, and F is the local optical fluence (J/m^2). Together, μ_a and F can be understood as the total energy deposition (J/m^3), or absorbed optical energy [6, 28, 40]. Equation 1 shows that the absorption coefficient of an object can be determined from pressure measurements if the optical fluence is known.

1.3. PAI Implementation: Tomography, Microscopy, and Endoscopy

The principles of PAI have been primarily adapted in major forms to photoacoustic microscopy (PAM), photoacoustic tomography (PAT), photoacoustic computed tomography (PACT), and photoacoustic endoscopy (PAE) [46]. These configurations are represented schematically in Figure 3 and summarized in Table 1. PAI systems may operate in reflection (backward) mode or transmission (forward) mode [47]. In reflection mode, the irradiation source and transducer are on the same side of the sample. The irradiation source and transducer are typically coupled, making operation similar to B-mode ultrasound imaging. In forward mode, the irradiation source and transducer are on opposite sides of the sample. This mode is usually limited to thin tissue sections or *ex vivo* samples because of the strong attenuation of light through tissue.
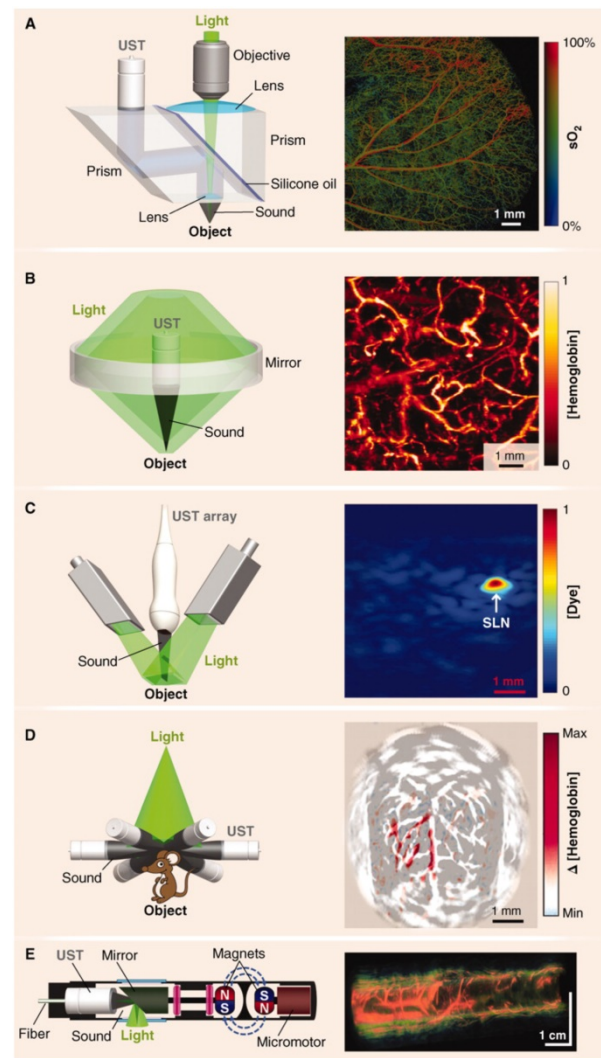
PAM is a reflection or transmission mode technique in which a single element transducer raster scans the sample and it is capable of millimeter imaging depths and micron resolutions[48]. In this mode, the optical excitation and acoustic detection create dual

foci that are both focused to increase sensitivity [3]. A single laser pulse is capable of returning a 1D ultrasonic signal with resolution axial to the laser. When scanning laterally, the laser transduces these signals across the area of the sample, generating 3D images. Axial resolution depends on the acoustic time of flight and lateral resolution relies on the distance between foci [3]. PAM is further classified by the modality that governs resolution: OR-PAM (optical resolution) or AR-PAM (acoustic resolution). OR-PAM is limited in depth by the optical diffusion limit (~1.2 mm), but can image cellular and subcellular structures from hundreds of nanometers to a few micrometers [49, 50]. The capabilities of OR-PAM have recently been extended by Lan et al., who reported frame rates of 900 Hz with a wide field of view (12 mm) using a hexagon-mirror scanner [51, 52]. AR-PAM uses dark-field optical excitation, and is capable of penetrating millimeters beyond the diffusion limit (though this depth sacrifices lateral resolution) [53]. A 45-µm lateral resolution and 3-mm imaging depth are achievable values for AR-PAM [3]. PAM systems are typically benchtop configurations that are most conveniently used for *ex vivo* applications; however, they can certainly be used for *in vivo* work. For example, subcutaneous melanomas in mice, oxygen saturation in rats, and total hemoglobin concentration in the human palm have been imaged with PAM [48]. Furthermore, a handheld PAM probe using a waterproof MEMS scanner (total weight: 162 g, diameter: 17 mm), was recently developed and shown to be effective for clinically relevant, *in vivo* applications such as delineating the 3D boundaries of a human mole [54]. These miniaturizations will improve the clinical feasibility of PAM systems.

PAT is a technique that follows the principles described in Section 1.2— it is widely used in research studies and multiple commercial systems are on the market. In focused scanning PAT, a focused ultrasonic transducer mechanically scans the area of the sample. PACT was developed to decrease the long imaging times (tens of minutes for a full mouse body) associated with such raster scanning modes [28]. It implements a wide beam of homogenous light to illuminate the entire region of interest and an array (linear or circular) of ultrasound detectors for signal acquisition. Back-projection algorithms are then used to pinpoint the ultrasonic sources and reconstruct 2D or 3D images [55]. PACT is faster than scanning PAM and can image more deeply, but typically has lower resolution [28]. In general, tomographic systems have resolutions in the 0.1 – 1.0 mm range but can achieve multiple centimeter imaging depths in soft tissue. Another advantage of tomography is that transducers (e.g. linear arrays) can be handheld, as in conventional ultrasound imaging. A recently published review covers advancements in handheld PAI in detail [56].

Figure 3. Major hardware configurations for PAI. (A) OR-PAM of oxygen saturation in a mouse ear. The light source is focused by an objective lens and sound is focused by a concave lens at the bottom of the prism where it is reflected to the ultrasound transducer (UST). (B) AR-PAM of hemoglobin concentration in a human palm. Dark-field illumination creates a cone of light rather than a point. (C) Linear Array PACT of methylene blue localized to a rat sentinel lymph node. Diffuse homogenous light illuminates the sample and is collected by a scanning line of transducer elements. (D) Circular Array PACT of cerebral [hemoglobin] dynamics. The array of ultrasound transducers can detect acoustic waves generated by the sample in all directions of a given plane. (E) PAE of a rabbit esophagus where components have been miniaturized for internal imaging. Adapted with permission from [3], copyright 2012 AAAS.

PAE has also been developed for imaging in difficult locations such as the gastrointestinal tract, lungs, trachea, and mediastina [57]. These internal organs can be imaged using miniaturized components confined to the tip of an endoscopic probe a few millimeters in diameter [58, 59]. In such cases, typically an apparatus combining the light generator (optical fiber) and ultrasound detector is driven by motors to circumscribe the target resulting in cross-sectional and volumetric images. The size and capabilities of these PAE probes will improve as

designs using optically transparent transducer components become more common and are further miniaturized. Intraoperative PAE applications are discussed more in Section 2.1.

1.4. Strengths and Limitations of PAI

PAI demonstrates numerous unique features and advantages over traditional imaging techniques. For example, by relying on NIR and visible light, PAI eliminates the risks associated with high-frequency ionizing radiation. It is capable of imaging at multiple scales, resolving single cells, organelles, and capillaries *in vivo* [61, 62]. In PAM, imaging depths and resolutions can be scaled from the micro to macro regime by tuning the numerical aperture of the objective lens or the central frequency of the transducer [3, 4]. Unlike most optical imaging techniques, PAI is capable of breaking the optical diffusion limit, which is defined by the transport mean free path (~1 mm in tissue) [63]. Photons scatter ballistically above this depth and diffusely below it. Most optical techniques cannot achieve adequate resolution below this depth, but PAI overcomes this limit by detecting the ultrasonic waves induced by diffuse photons [46]. This fact demonstrates that PA signal is fundamentally based on absorption (and subsequent thermoelastic expansion). In effect, background can be reduced in PAI because non-absorbing objects do not generate PA signal and spectral imaging/signal thresholding can be used to minimize signal from endogenous absorbers.

Both non-fluorescent and fluorescent targets can be imaged, and a number of endogenous chromophores have strong signal such as oxygenated/deoxygenated hemoglobin [64], melanin [65], lipids [66], and water because of their differential absorbance spectra in the NIR. A wide variety of exogenous contrast agents have also been developed and are designed to boost contrast while expanding the range of biological processes that can be imaged. Some examples include small-molecule dyes, metallic and polymeric nanoparticles, up-conversion nanoparticles, carbon nanotubes, microbubbles, quantum dots and numerous others [7, 67, 68]. Because a diverse array of materials and strategies have been investigated as contrast agents, it can be useful to distinguish them according to certain traits: for instance, activatable vs. non-activatable (passive), nanoparticle vs. small-molecule, inorganic vs. organic, or NIR-I absorbing vs. NIR-II absorbing. Activatable probes benefit from higher specificity and signal-to-background ratios than passive ones because they only activate PA signal following a biological stimulus. Nanoparticles are ideal for carrying cargoes and have unique optical properties, but small-molecules tend to have better biocompatibility and lower toxicity/faster clearance. Similarly, organic nanomaterials offer better biodegradability than inorganics, but may have lower absorption coefficients or more complex syntheses.

One important consideration for nanoparticle design is the size: typically, particles < 6 nm will be rapidly cleared by the kidneys, whereas particles > 8 nm cannot undergo glomerular filtration, and sizes between 30-200 nm can achieve long circulation times for enhanced accumulation and retention in tumors [69, 70]. It is also known that for photothermally active gold nanomaterials (e.g. spheres, rods, shells), the magnitude of extinction increases with size (e.g. from 20 to 80 nm for spheres) [71]. Specifically, the contribution of scattering to the total extinction increases relative to absorption. Feis et al. investigated this effect with gold nanoparticles and saw that larger particles at larger wavelengths had lower photoacoustic amplitudes than predicted by the extinction spectrum [72]. This discrepancy was attributed to the insensitivity of PAI to scattering effects. Therefore, the individual contributions of absorption and scattering, which is often size dependent, should also be considered during PA nanoparticle design. Overall, desirable properties for effective contrast agents include high molar absorption coefficients, absorption at long NIR wavelengths (ideally non-overlapping with endogenous absorbers), stability, affordability, targetability, and safety [10].

Using exogenous contrast, imaging depths in PACT have been reported as high as 11.6 cm in chicken breast tissue and 5 cm in the human arm [73]. However, deep imaging (>1 cm) with high resolution still remains a challenge for most PA applications. Specific deep-lying organs that present challenges for PAI because of their location include the heart (location under the rib cage), lungs (beneath rib cage and gas-tissue interface), stomach (a hollow structure and under rib cage), and pancreas (depth) [28]. Penetration depth issues can be countered, however, with exogenous agents (especially in the second optical window) and unique hardware designs. For example, novel transducers and intraoperative probes have been designed to image trans-vaginally [74], trans-rectally [75, 76], and trans-esophageal [77]. Of course, all hardware designs can be combined with molecular imaging strategies using exogenous contrast agents to maximize performance (see Table 2 for representative molecular imaging agents). Furthermore, one of the emerging trends in recent years has been the increased use of the second optical window (NIR II: 1000-1700 nm) for fluorescence imaging and subsequently PAI [78, 79]. This range is highly attractive for biophotonic applications because

of the diminished light-tissue interactions — specifically, scattering and autofluorescence — at longer wavelengths [80]. Compared to the first optical window (650-950 nm), these factors allow imaging at higher penetration depths. Additionally, because these photons have lower energies, the maximum permissible exposure (MPE) is higher for clinical applications which can boost PA performance and reduce signal-to-background ratios. The first NIR-II PA contrast agents explored have been inorganic nanomaterials, such as plasmonic precious metal nanoparticles and copper sulfide nanoparticles [81-83]. However, recent progress has been made in organic NIR-II probes, including semiconducting polymer nanoparticles [22, 79] and small molecules [19]. Still, the second optical window presents new challenges that must be overcome. For example, water has a significant absorption peak at 1450 nm, existing NIR-II agents have low quantum yields, and few organic materials have been reported that can absorb above 1064 nm in the NIR-II [22].

2. Metastastis Detection & Surgical Resection

2.1. Endogenous Targets for Guided Surgery

A substantial portion of PAI research is devoted to cancer applications. The vast majority of cancer deaths are caused by metastatic progression of the disease. To mitigate these cases, it is important to determine both the extent of metastasis and the margins of tumors to guide surgical intervention [84]. Intraoperative PAI shows potential to improve upon existing methods (immunohistochemistry, histopathological assessment) by determining these variables in real time. Many groups are investigating the potential for PAI to detect metastasis and enhance tumor imaging. Melanoma is an appropriate target for such studies because melanoma cells contain highly absorbent melanin that acts as an endogenous PA absorber.

Using PAT, Grootendorst et al. compared intraoperative PA images of melanoma metastases from resected, human sentinel lymph nodes (SLN: the first lymph node to which a tumor drains) to hematoxylin-eosin histologic images (the routine method for prognosis that takes days). This showed that intraoperative detection of melanoma was possible although distinctions between malign and benign nodes were not obvious [85]. In order to discriminate between signals from blood versus melanin, the signal from *ex vivo* nodes were characterized spectrally and separated with an unmixing algorithm [86]. However, the accuracy of this method depends entirely on the accuracy of the PA reference spectra measured for blood and melanin. The potential benefit of intraoperative PAI of *ex vivo* SLNs is that detection of metastasis would allow an immediate node dissection and prevent the need for a second surgery. Luke & Emelianov showed that metastasis in lymph nodes from other (non-melanoma) primary tumor types could also be imaged [87]. In a mouse model for oral cancer, they took advantage of the decreased blood oxygen saturation (SO_2) associated with metastatic foci in SLNs and imaged deoxygenated/oxygenated hemoglobin to evaluate the metastasis. The differential absorption between oxygenated and deoxygenated blood provides one of the most straightforward mechanisms of endogenous PA contrast [64, 88, 89].

Table 2. Representative exogenous contrast agents used for applications in PA-image guided surgery.

Photoacoustic Agent	Description	Wavelength (nm)	Target	Image-Guided Outcome	Reference
B7-H3-ICG	Anti-B7-H3 conjugated with Indocyanine Green	800-825	Breast Tumor	*In vivo* murine tumor delineation	Wilson et al. 2017 [104]
Gold Nanorods	Gold nanorods coated with PEG, 41 nm x 12 nm, 3.5 aspect ratio	756	Ovarian Tumor	*In vivo* murine tumor delineation and resection guidance	Jokerst et al. 2012 [105]
Iron Oxide NPs (Endorem®)	Superparamagnetic Iron Oxide NPs (80-150 nm diameter)	720	Lymphoma	Nodal staging of resected human lymph nodes	Grootendorst et al. 2013 [106]
Coomassie Blue Polyacrylamide NPs	Polyacrylamide hydrogel nanoparticles crosslinked with Coomassie-Blue dye (80 nm diameter)	590	Brain Tumor	*Ex vivo* murine tumor delineation	Ray et al. 2011 [107]
ICG-Coated Gold Nanorods	Gold nanorods coated with liposomal indocyanine green, 31 nm x 10 nm, 3.1 aspect ratio	795	Liver Tumor	Pre-operative PA detection and intraoperative fluorescence-guide resection	Guan et al. 2017 [108]
Black Hole Quencher 3-Fluorescein-labeled Trastuzumab	Chemotheraeutic trastuzumab dual-labeled with BHQ3 (photoacoustic) and fluorescein (fluorescence)	700	Breast Tumor	Pre-operative PA detection and post-operative fluorescence-guided resection validation	Maeda et al. 2015 [109]
Silica-coated gold nanoparticles with Raman/MRI-active layers	Gold nanoparticles (60 nm) coated with trans-1,2-bis(4-pyridyl)-ethylene (Raman), silica, and DOTA-Gadolinium (MRI)	532	Brain Tumor	Intra-operative PA and Raman-guided resection	Kircher et al. 2012 [110]

To accelerate clinical translation, intraoperative handheld PA probes have been designed that streamline operation of the technology. Xi et al. demonstrated a handheld microelectromechanical systems (MEMS) probe for real time inspection of 3D tumor margins in mice during resection [90]. Here, they used the imaging system at 532 nm to evaluate the completeness of tumor removal following surgery and histologically validated the margins as measured with photoacoustics with < 6.5% error. One issue with using endogenous contrast for resection validation, especially at 532 nm, is the strong absorption of blood, which will produce background during surgeries. Longer wavelengths can mitigate this effect but it is difficult to match the signal to background ratios achievable with exogenous agents.
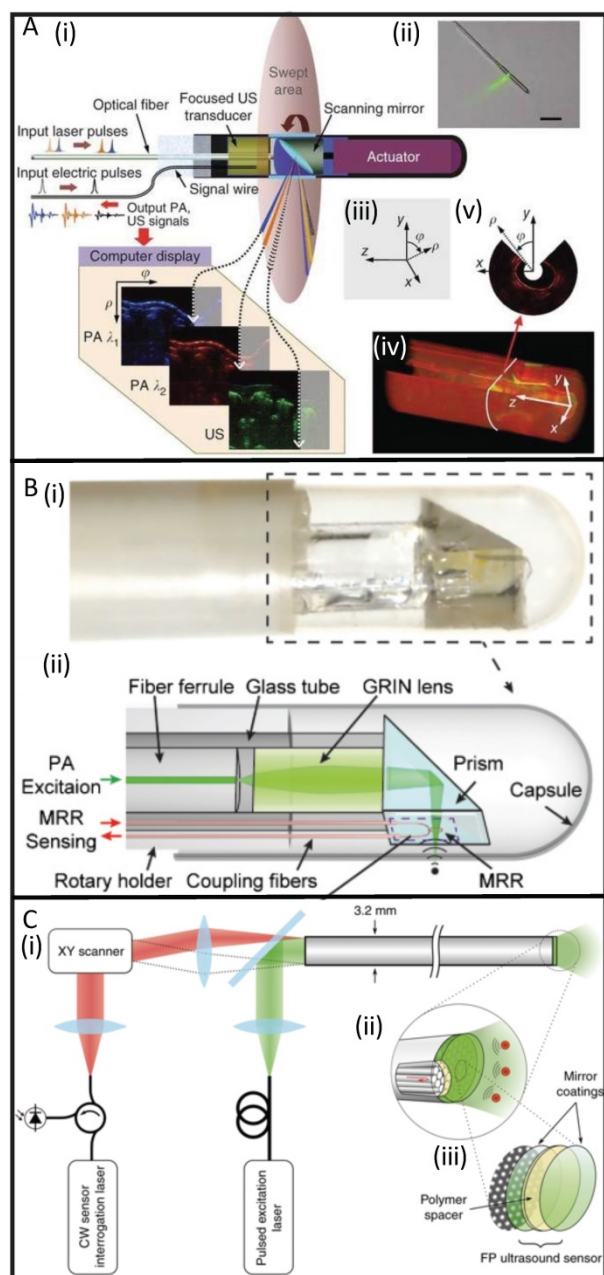
Neuschmelting et al. evaluated both 2D and 3D handheld MSOT (multispectral optoacoustic tomography) devices developed by iThera Medical by imaging murine brain melanomas at 4 MHz and 700 – 900 nm [91]. The authors implanted B16F10 melanoma cells into the right frontal lobe, where tumors 3.5 – 7.0 mm in diameter grew within 13 days; the size of these tumors were independently measured with MRI. The 2D system was deemed more accurate (bias = 0.24 mm) than the 3D system (bias = 2.35 mm) but was limited to axial tumor depths of 4 mm. The 3D probe was limited by tumor size (< 3.5 mm) in all dimensions, but the acquisition time was shorter. The performance disparity between the 2D and 3D systems was attributed to a non-ideal distribution of diffused light in the transducer array of the 3D system. These handheld systems also showed superior signal to noise ratios and limits of detection and for metastatic melanoma cells (5 cells/uL at 8 mm tissue depths in mice) to PET/CT using fluorine 18 fluoro-deoxyglucose [92]. However, this sensitivity would be difficult to achieve if applied to human lymph nodes located centimeters below the skin. Additionally, to our knowledge, these systems have not yet been used to monitor resection during or after an operation.

Miniaturized and endoscopic probes can offer advantages for image-guided surgeries due to their adaptability and form factor. One example is radical prostatectomy, a common treatment for prostate cancer in which the prostate and seminal vesicles are fully removed [93]. Oncological success (full tumor elimination) must be balanced with minimizing functional damage (e.g. incontinence and impotence). A recent study was conducted to determine the best scanning geometry for intraoperative PA prostate imaging [94]. It was demonstrated through simulation and experiment (using phantoms) that a convex, "pick-up" transducer (28 mm width, 10 MHz) controlled by a da Vinci robot was a promising approach for prostate imaging. In this setup, the transducer is located anterior to the prostate and can form a cylindrical detection surface while conformally scanning the prostate to generate a 3D image. The integration of PAI with a da Vinci robot for guided surgery was also investigated by Gandhi et al [95]. They used phantom studies to show that by connecting an optical fiber (powered by a pulsed laser diode) to a surgical arm of the robot, and a transducer to another arm, that the system could distinguish separation distances blood vessels and nerves in real-time while also visualizing the tool tip itself[96]. These technologies are still in their early stages, but show promise for improving patient outcomes during future *in vivo* and human studies.

PAE applications have been studied for over a decade, but miniaturizing the hardware while maintaining high image quality is a challenge. Nevertheless, systems have been proposed and constructed for detection of atherosclerotic plaques in cardiovascular disease [97-100], esophageal imaging [101], and gastrointestinal diseases [58]. However, many of these designs take a side-viewing approach, whereby a single element transducer is attached to the distal end of an optical fiber and generates a field of view perpendicular to the fiber axis. This approach is not as desirable as a forward-viewing design, which is more useful for image-guided intraoperative procedures [102]. For PAE, this presents a design challenge because forward-viewing necessitates either lateral scanning of the transducer head (which is more challenging then rotational scanning of a side-view design), or the use of a 2-D array of transducer elements. Unfortunately, traditional ultrasound transducer elements are opaque to light; therefore, they need to be offset from the light source which increases the overall probe size.

To solve this issue, optically transparent ultrasound elements can be used. Dong et al. used a polymeric microring resonator ultrasound sensor and demonstrated phantom imaging with sub-10- µm axial resolution and 15.7 µm tangential resolution but retained a side-view design [103]. Furthermore, Ansari et al. recently demonstrated a novel, forward-view PAE system with a 3.2 mm diameter footprint that uses a Fabry-Pérot polymer film sensor, capable of resolving microvascular anatomy in impressive detail [60]. The sensor acts as a high-density transducer array with 50,000 individual elements and allows transmission of light with 45-170 µm on-axis lateral resolution, 31 µm vertical resolution, and 1-7 mm imaging depths. While still in its early stages, this new class of instrumentation shows promise for accelerating the use of PAE in image-guided laparoscopies and surgeries (Figure 4).

Figure 4. Developments in PAE instrumentation. (A) A side-viewing photoacoustic endoscope with 3.8 mm diameter (i, ii) that uses a conventional single-crystal transducer (LiNbO3, 36 MHz) and achieves circumferential scanning with a rotating mirror that reflects ultrasound waves and laser pulses. Representative images from rabbit esophagi with Cartesian and cylindrical coordinate systems (iii) are shown in (iv) and (v) [58]. (B) A photograph (i) and schematic (ii) of a side-viewing endoscope (4.5 mm diameter) that uses an optically transparent, micro-ring resonator transducer. [103]. (C) A schematic of a forward-viewing endoscope with 3.2 mm diameter that uses an optically transparent Fabry-Pérot ultrasound sensor attached to the distal end of the device. A magnified view of the distal end (i) shows individual fiber-optic cores beneath the Fabry-Pérot sensor which is revealed in (iii): it is made from two dielectric mirror coatings that sandwich a Parylene C polymer spacer (15 μm) [60].

2.2. Exogenous Contrast Agents for Guided Surgery

Many exogenous contrast agents have been designed to accumulate at target sites and enhance the photoacoustic signal of diseased tissues. These are typically small molecules or nano-scale agents injected into the bloodstream, but they can be administered via other routes. This section highlights some of the vehicles used specifically for tumor identification and resection (Table 2).

Variations of gold nanoparticles are popular because of their strong optical absorption (orders of magnitude greater than organic dyes), and geometry-dependent resonant frequencies that exploit the NIR window [13, 14]. Gold nanorods were employed in 2012 as dual PA/Raman contrast agents for passive targeting of ovarian xenografts in mice [105]. Here, maximum PA signal was observed after 3 h (persisting for 48 h). The detection limit was 0.40 nM, and the margins between tumor and normal tissue were clearly visualized. Silica-coated gold nanoparticles coated with Raman and MRI-active layers have also been developed as triple modality (PA/MRI/Raman) contrast agents for glioblastoma tagging and resection, shown in Figure 5 [110]. They exhibited optical absorbance coefficients 200-fold higher than previously studied carbon nanotubes, allowing for 3D imaging of deep-lying tumor tissue (via PA) in conjunction with the Raman modality's high sensitivity to microscopic tumor deposits. Guan et al. combined gold nanorods with indocyanine green dye (ICG, a NIR absorbing fluorescent dye) to integrate fluorescent imaging and photoacoustics with utility for liver cancer diagnosis [108].

A variety of other nanoparticles for PA-based tumor tagging have been studied as well [8]. Magnetic iron oxide nanoparticles (IONPs) are biodegradable with low toxicity and have been used previously in humans in conjunction with MRI [111]. They enhance PA signal in lymph nodes following uptake by nodal macrophages although metastatic versus benign tissue could not be distinguished [106]. However, Xi et al. reported the successful imaging of breast cancers with IONPs conjugated with NIR-dye labeled peptide fragments in a murine model [112]. Other groups have reported tumor targeting antibodies labeled with PA contrast agents (such as the Black Hole Quencher 3 dye) [109] and self-assembling nanovesicles containing lipid-based dyes (J-aggregates) [113].

One challenge in PAI is differentiating the signal from the contrast agents from that of endogenous photoabsorbers. With spectroscopic photoacoustic imaging (sPA), it is possible to reduce noise from background photoabsorbers using knowledge of their wavelength-specific absorption spectra and relative tissue concentrations to isolate the signal of the exogenous agent [114, 115]. Wilson et al. used sPA and an ICG-labeled antibody to target and image a novel breast cancer surface receptor, B7-H3 [104]. They could distinguish agent that had located and

penetrated the target cells because of the spectral shift in absorption following its endocytosis and degradation by malignant cells.

3. Monitoring Drug Delivery

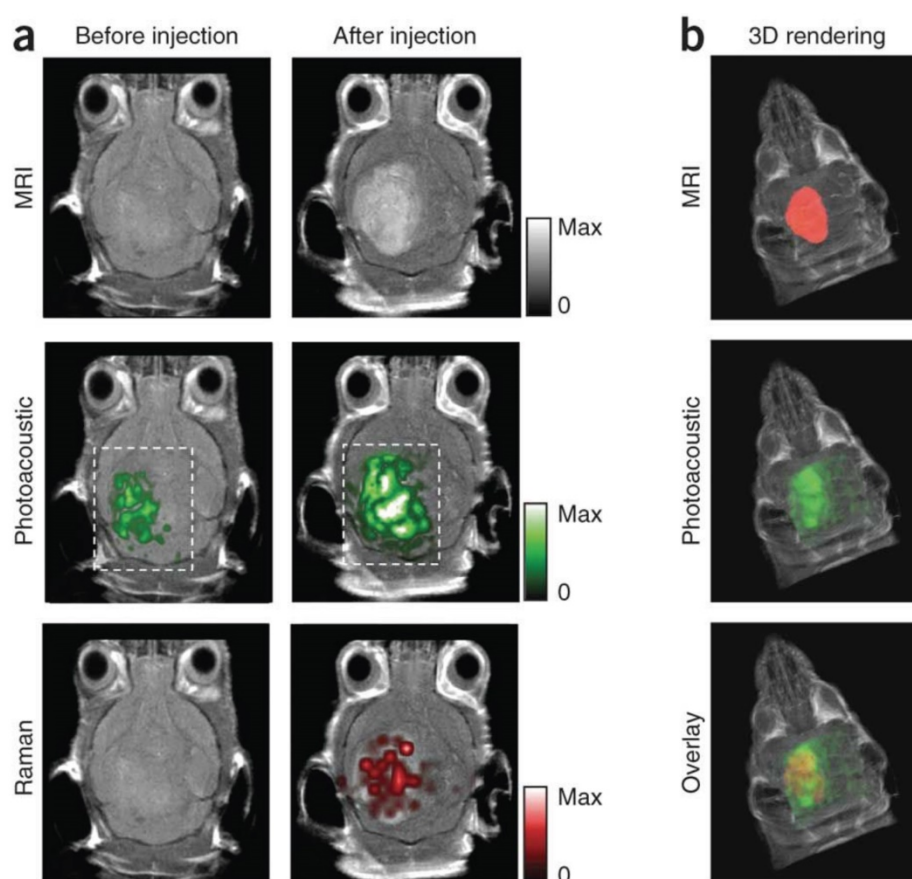## 3.1. Nanocarriers and Co-Loaded Contrast Agents

A major challenge in drug delivery is the noninvasive and real-time monitoring of biodistribution and pharmacokinetics. In humans, radiotracers in conjunction with PET/CT scanning can be used [116]. In animals, pharmacokinetics are usually determined via radiolabeling followed by dissection or imaging for biodistribution analysis [117]. PAI shows potential in small animals for both localized drug monitoring and whole-body imaging in a non-invasive format without ionizing radiation [118]. Unfortunately, very few clinically prescribed drugs, if any, exhibit intrinsic absorption in the NIR—an important trait for PAI [28]. This shortcoming can be overcome, however, with the use of co-loaded contrast agents and nanocarriers and that act as vehicles for drugs. Furthermore, some of these materials can act therapeutically themselves, in the case of photothermal and photodynamic therapies. Examples of contrast agents discussed in this section are highlighted in Table 3.

In 2011, hollow gold nanocages were loaded with a phase change material (1-tetradecanol) and either methylene blue (44 g/L solubility in H_2O) or Rhodamine 6G (20 g/L solubility in H_2O) to demonstrate a controlled release drug delivery system that can be monitored with PAI [123]. 1-Tetradecanol has a melting temperature of 38°C and the authors showed that high-intensity focused ultrasound (HIFU) or heating could melt the material, allowing both the hydrophilic methylene blue and 2-fold less hydrophilic Rhodamine 6G to leak from pores in the nanocages at a controllable rate. Another group has shown that the hydrophobic cancer drug, doxorubicin, can be loaded with fucoidan capped gold nanoparticles for PA imaging of anti-tumor therapy in breast cancer cell lines [124]. However, it was not demonstrated *in vivo*. One interesting approach is to use the pulsed NIR excitation itself as a stimulus for drug release—e.g. using a low laser fluence for imaging and a higher fluence for triggered release. Wilson et al. first developed this platform by loading phase-change particles (perfluorocarbon droplets) with gold nanorods (for optical absorption), showing that both US and PA signal could be drastically boosted following the vaporization of the particles; the technique was then extended by Zhong et al. who incorporated paclitaxel for an activatable release mechanism at a laser fluence of 14 mJ/cm² [125, 129]. Organic vesicle-forming carriers also show potential for drug delivery imaging via their capacity for passive loading and biodegradability. Supramolecular assemblies of the highly absorbent porphyrin (porphysomes and porphyrin shell microbubbles) can accumulate in tumors of xenograft-bearing mice while exhibiting high contrast [130, 131]. Ho et al. showed that polymeric nanoparticles containing porphyrinoids could boost PA signal upon complexing with uranyl ions, demonstrating a path towards sensitive and specific imaging of radioactive isotopes *in vivo* [126].

Table 3. Representative exogenous PA contrast agents with applications in drug delivery and monitoring.

Photoacoustic Agent	Description	Wavelength (nm)	Target	Image-Guided Outcome	Reference
Semiconducting Polymer Nanoparticles	Photothermal SPNs doped with fullerene	750	Breast Tumor	Photothermal therapy	Lyu et al. 2016 [119]
Nanonaps	Frozen micelles of hydrophobic, napthalocyanine dyes (~20 nm diameter)	600, 707, 793, 863 (Tunable)	Intestine	Diagnosis/treatment of intestinal motility disorders	Zhang et al. 2014 [120]
MoS₂ Nanosheets	PEGylated, 2-D nanosheets loaded with photodynamic Ce6	800	Breast Tumor	Photothermal therapy, photodynamic therapy	Liu et al. 2014 [121]
RbₓWO₃ Nanorods	Rubidium tungsten bronze nanorods with doxorubicin payload, 20-40 nm x 5 nm	808	Breast Tumor	Combined chemo/photo-thermal therapy	Tian et al. 2014 [122]
Gold Nanocages	Gold nanocages loaded with 1-tetradecanol (phase-change) and organic dyes	750	Non-specific	HIFU/Temperature-triggered drug release and monitoring	Moon et al. 2011 [123]
Fucoidan Capped Gold Nanoparticles	Gold nanoparticles coated with fucoidan and doxorubicin	566	Breast Tumor	Chemotherapy	Manivasagan et al. 2016 [124]
Perfluorocarbon Nanodroplets	Perfluorocarbon nanodroplets loaded with gold nanorods and paclitaxel	770	Cervical Tumor	Combined chemo/photo-acoustic therapy	Zhong et al. 2016 [125]
Porphyrinoid-Loaded PLGA Nanoparticles	Poly(lactic-co-glycolic) acid nanoparticles loaded with porphyrinoid macrocycles	910	Uranium	Quantification of in vivo uranium exposure	Ho et al. 2015 [126]
Optode Nanosensors	Intradermal injectable nanosensor containing a crown ether ionophore and a chromoionophore	515, 660	Lithium	Drug monitoring of systemic lithium dose	Cash et al. 2015 [127]
Methylene Blue or Nile Blue	Cellulose-based, PEG-infused substrates containing Nile Blue	680	Heparin	Drug monitoring of systemic heparin dose	Jeevarathinam et al. 2018 [128]

Figure 5. Murine brain tumor imaged *in vivo* with modified gold-silica nanoparticles for PAI, MRI, and Raman spectroscopy for guided surgery. (A) Tumor-bearing mice were given IV injections of the particles and imaged axially in 2D both pre- and post-injection at 2 h (PA), 3 h (Raman), and 4 h (MRI). PA and Raman images were overlaid with MRI demonstrating clear tumor visualization and co-localization between techniques. (B) 3D construction of MR with segmented tumor (red: top), 3D PA overlay with MRI (green: middle), and overlay of segmented tumor, PA, and MRI (bottom). Adapted with permission from [110], copyright 2012 Nature Publishing Group.

Another promising method for direct PA drug monitoring was demonstrated by Cash et al. in 2015 [127]. They developed a nanosensor capable of detecting systemic lithium. Upon recognition by a crown ether ionophore, a lithium cation deprotonates a chromoionophore of the nanosensor, changing its absorption, PA, and fluorescence properties. This injectable nanosensor allows for the continuous PA and fluorescence monitoring of lithium, which has both a narrow therapeutic window and low toxic dose (Figure 6). An injectable nanosensor has also been developed for cell permeable calcium ion imaging [132]. This group synthesized a metallochromic compound based on fura-2, a fluorescent indicator for calcium, but replaced the chromophore with a semi-cyanine chromophore to shift the absorption to longer wavelengths while maintaining a photoinduced charge transfer mechanism. Furthermore, the first application of photoacoustics for non-invasive imaging of the ubiquitous anticoagulant, heparin, was recently reported [128, 133, 134]. Currently, heparin concentrations in patients undergoing surgery are monitored with the activated partial thromboplastin time (aPTT) per nomogram, an *in vitro* surrogate test

for the deactivation of clotting factors [135]. Here, the concentration of heparin was monitored in blood using the FDA approved dye methylene blue, a method that benefits from a fast turnaround time, strong sensitivity to heparin, and correlation to the aPTT. Methylene blue is an attractive PA agent because of its clinical approval [136, 137] — it has previously been used for PAI of sentinel lymph nodes [138] and has also demonstrated PA lifetime and intensity shifts via self-quenching and interactions with micelles [139, 140].

Non-IR-absorbing carriers can be used for drug monitoring if the payload includes fluorescent/PA-active dyes. Multispectral Optoacoustic Tomography (MSOT) was developed to image fluorescent proteins *in vivo*. It can track, at high speeds, the biodistribution of fluorescent agents (e.g. ICG, carboxylate dyes) through circulation and uptake in the liver, gallbladder, and kidneys [141, 142]. These agents are commonly loaded within delivery vehicles to boost contrast. Perfluorocarbon (PFC) nano-droplets have been loaded with ICG to enable photoacoustic and ultrasound imaging; signal is enhanced by the optically triggered phase transition of the droplets to

generate PFC microbubbles [143]. This controlled event also allows for drug release. Another unique example is the use of PAT with micelle-forming naphthalocyanines, "nanonaps", to address the challenges of non-invasive GI tract imaging [120]. These hydrophobic chromophores self-assemble in biocompatible surfactant (PEO-PPO-PEO) to form 20 nm spheres with high PA signal. Organic dyes are promising in PAI for their biocompatibility, multimodal nature, small size, and general stability. Current efforts devoted to synthesizing new fluorophores for optical imaging in the deep NIR (second optical window) will also have significant utility for PAI [144] For the time being, payload strategies that incorporate already FDA approved dyes such as methylene blue and ICG may have the quickest path to clinical approval. However, much work remains towards demonstrating the full potential of PAI for drug delivery and monitoring. In humans, because penetration depths are heavily surface-weighted and tissue-transducer coupling is required, it is likely that drug monitoring applications will continue to take the form of localized imaging and monitoring approaches rather than full-body biodistributions.
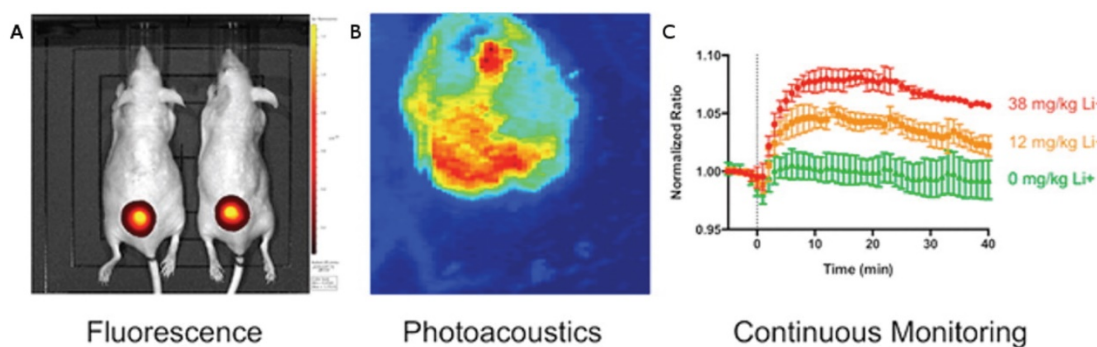
3.2. Photothermal Contrast Agents

Certain nanocarriers can exert their own therapeutic effects by exciting them via NIR laser radiation to release heat. Photothermal therapy (PTT) refers to the use of these photothermal agents for targeted tissue ablation. In recent decades, thermal ablation has been used to destroy diseased tissue using radiofrequencies [145] and lasers without contrast agents [146]. Recently, dual contrast/PTT agents have become attractive for their ability to combine diagnostic and therapeutic capabilities into a single agent [147]. Desirable traits for these agents include the ability to locate and identify tumor margins, monitor the treatment in real time, and determine post-treatment effectiveness afterwards. Photoacoustic imaging is particularly suited for monitoring these tasks.

In 2006, gold nanorods functionalized with antibody were shown to selectively target malignant cells *in vitro* [148]. Photothermal destruction of the cells could be triggered using an 800 nm NIR laser, and malignant cells (with higher nanorod uptake) required half the laser power of non-malignant cells to cause necrosis. It was subsequently shown that PTT could be integrated with PAI using agents such as quantum dots [149], graphene [150], gold nanoshelled microcapsules [151], gold nanovesicles [152], iron oxide-polydopamine nanocomposites [153] porphy-somes [130, 154], and semiconducting polymers [119]. Quantum dots extended their application in fluorescent imaging to PAI/PTT, but their absorption spectra marginally overlapped with that of blood. In contrast, nanographene sheets (coated with polyethylene glycol, "PEGylated") showed excellent NIR absorption and passive targeting of tumors, while requiring a relatively low laser power density for effective ablation.

Transitional metal dichalcogenides (TMDCs) are another noteworthy class of 2D nanomaterials; they have gained popularity in electronics and energy storage because of their unique optical and electronic properties. These materials are now being studied for their utility in medicine. In one such example, PEGylated WS$_2$ nanosheets passively targeted tumors while maintaining strong photothermal activity. This enabled tumor ablation via NIR light-activation [155]. Both groups hypothesized that the 2D geometries of nanosheets are well suited to take advantage of the experimentally observed enhanced permeability and retention (EPR) effect of growing tumors.

Fluorescence   Photoacoustics   Continuous Monitoring

Figure 6. Photoacoustic and fluorescent monitoring of systemic lithium concentration *in vivo* using injected bimodal nanosensors. (A) NIR fluorescence was used to image lithium concentration at the site of subcutaneous nanosensors administration. (B) Photoacoustic tomography shows the boundary of the subcutaneous nanosensor injection. (C) Photoacoustics and fluorescence were both used to measure nanosensor activation. Dose-dependent curves show continuous monitoring demonstrating that higher lithium concentrations yielded stronger signal. This also revealed that peak lithium was achieved at 18 min. Adapted with permission from [127], copyright 2015 American Chemical Society.
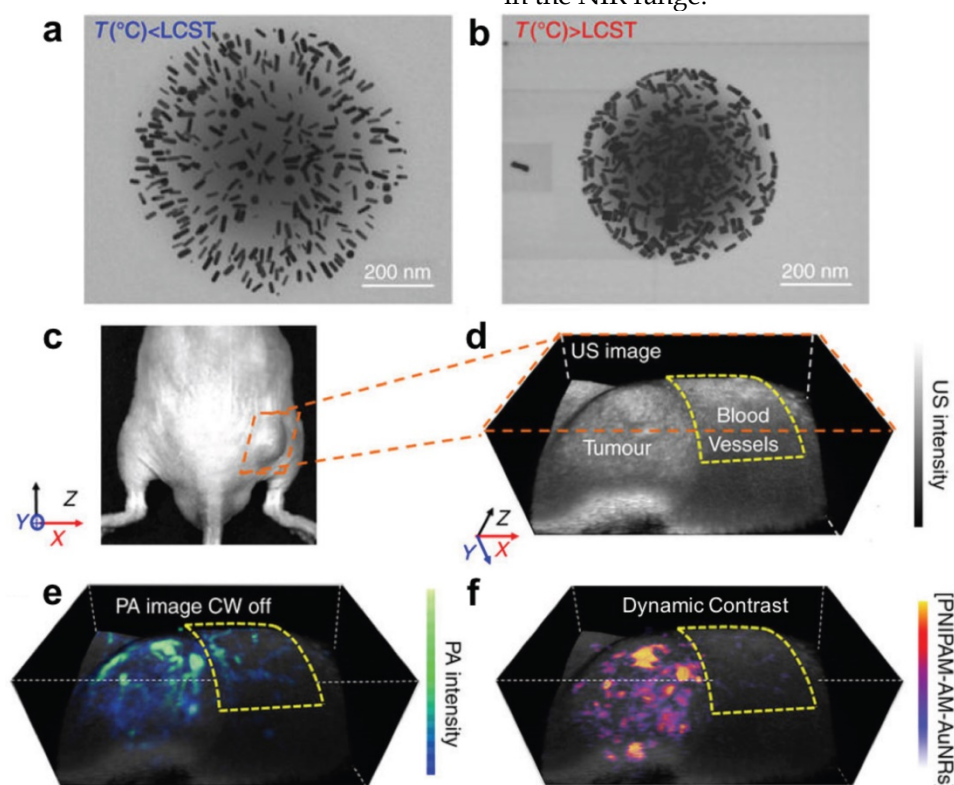
Organic carriers can also be useful in PTT for their biocompatibility and capacity for drug loading. Porphysomes have passive tumor targeting and PA signal while also being photothermally active [130, 154]. Some polymer carriers have been combined with inorganic components: gold-nanoshelled microcapsules, for example, consist of poly-lactic acid cores coated with gold nanoparticles to impart both photoacoustic and photothermal functionality with drug-loading capabilities. Recently, semiconducting polymer nanoparticles, engineered at the molecular orbital level to favor photoinduced electron transfer, were shown to localize in tumors while increasing photoacoustic signal and PTT efficiency [119].

In 2017, the temperature responsive polymer poly(N-isospropylacrylamide) (PNIPAM), was loaded with photothermally active gold nanorods to achieve sensitive PA monitoring of photothermal therapy [156]. PNIPAM shrinks when heated, allowing the gold nanorods to approach one another and shift their NIR absorbance (and PA signal) via plasmonic coupling (Figure 7). These dynamic constructs were used to selectively monitor photothermal activation in murine prostate tumors while negating background from blood. Overall, these advances in PTT demonstrate practical ways that PAI can be leveraged with synergistic contrast agents to both deliver and monitor drugs in real time.

3.3. Photosensitizers and Photodynamic Therapy

Photodynamic therapy (PDT) is another therapeutic approach that can work in tandem with PAI. PDT was the first drug-device combination to be approved by the FDA over two decades ago [157]. It has been used clinically to address a wide range of conditions, such as acne [158], microbial infections [159], and macular degeneration [160]. Currently, researchers are showing the potential for PDT to address a number of unmet needs in cancer therapy [161]. It requires light, oxygen, and a photosensitizer, an agent that can absorb light and initiate a photochemical reaction to generate the highly reactive singlet oxygen, a type of reactive oxygen species (ROS). Singlet oxygen is characterized by the opposite spin of a pair of its electrons, reducing its stability and lending it cytotoxic effects. During the procedure, a photosensitizer is systemically or locally administered, localizing in a neoplastic region, followed by irradiation from a light source. Because NIR light penetrates tissue deeper than other optical wavelengths, ideal photosensitizers would be strong absorbers in the NIR range.

Figure 7. Gold nanorod (AuNR) loaded PNIPAM nanoparticles for PA monitoring of photothermal therapy. (A) Expanded form of PNIPAM-AuNRs below the lower critical solution temperature (LCST). (B) Compressed form of PNIPAM-AuNRs above the LCST, allowing plasmonic coupling between the gold nanorods. (C) Image of a prostate tumor in a mouse. (D) Ultrasound image of tumor with surrounding region of normal blood vessels highlighted. (E) PA image of tumor following injection of PNIPAM-AuNRs prior to photothermal heating (continuous wave (CW) laser off). (F) PA image with dynamic contrast following photothermal heating (CW laser on) where PNIPAM-AuNRs have compressed to shift their PA signal via plasmonic coupling and the pre-heating signal has been subtracted to remove the background from adjacent blood vessels. Adapted with permission from [156], copyright 2017 Nature Publishing Group.

PAI also uses NIR absorbing agents, and some photosensitizers exhibit PA contrast *in vivo*. This allows the monitoring of therapy in real time [162]. Ho et al. demonstrated the photoacoustic activity of five photosensitizers— the most promising molecule, zinc phthalocyanine, localized in tumors within 10 min, peaked at 1 h, and cleared after 24 h. Unfortunately, the activation absorption spectrum of many photosensitizers is in the visible range. In order to extend the usable depth of these agents in human tissue, it is possible to convert deep penetrating NIR light to visible wavelengths while enabling activation of the photosensitizers. Idris et al. accomplished this using mesoporous-silica-coated upconverting fluorescent nanoparticles that functioned as "nanotransducers" to convert NIR light to visible *in vivo* [163]. Creative strategies such as this one will be required to enable PDT in deep-tissue applications. Alternatively, because 1) PDT requires oxygen to generate ROS and 2) PAI can be used to image oxygen saturation (via the ratiometric absorption of oxygenated and dioxygenated hemoglobin), the efficacy of PDT can be monitored label-free. Shao et al. used AR-PAM to image SO_2 in the microvasculature of a rat ear following tail vein injection of the photosensitizer Verteporfin with 80 mW/cm^2 light irradiance for 60 min [164]. They observed an initial decrease in oxygenation followed by a gradual recovery during the treatment course; however, the data was limited to a sample size of n = 3. Nevertheless, this study showed the potential for PDT monitoring with endogenous contrast.

As with other PA applications, the therapeutic agent does not strictly require inherent contrast. The active agent (the photosensitizer, in PDT) can be loaded into NIR-absorbing vehicles to enable PA signal. Srivatsan et al. showed that the photosensitizer HPPH could be loaded onto the surface of gold nanocages via non-covalent entrapment with a PEG monolayer [165]. These conjugates were stable in saline and began to degrade in protein solutions. This allowed for slow release of HPPH under biological conditions. PAI was harnessed to track the progress of delivery and suppressed tumor growth in mice—likely because of the passive targeting of the nanocages and generation of singlet oxygen at tumor sites by HPPH. Similarly, gold nanovesicles loaded with the photosensitizer Ce6 have been shown to infiltrate tumors in xenograft-bearing mice while drastically reducing the growth of tumors after 14 d [166]. This study highlights the synergistic effects of agents that allow for both thermal ablation (PTT) and ROS generation (PDT). In fact, TMDC nanosheets, previously discussed for their photothermal applications, have also been employed for PDT. Liu et al.

took advantage of the high surface area of MoS_2 nanosheets to load Ce6, which then passively targeted and suppressed tumors via ROS generation and photothermal ablation [121]. One more strategy for synergistic therapy is to use a multifunctional material such as $Cu_2(OH)PO_4$ quantum dots to achieve a "one-for-all" technique for PAI-guided PTT/PDT [167]. Notably, these particles absorb well into the second optical window (up to 1700 nm). In the clinic, these could be implemented for image-guided therapy by delivering the agent to the site of a tumor, imaging the distribution of the agent for treatment guidance, and then pulsing NIR light for PTT/PDT therapy followed by PAI for short and long-term monitoring. However, the toxicological effects of quantum dots vary widely and more work is needed to establish their potential utility in humans [168].

4. Monitoring Disease States and Therapeutic Effects

Diseases are multi-scale processes that exert effects from the molecular to the visible. Diseases often begin with a molecular event and gradually cascade as larger macroscopic effects emerge. As a molecular imaging modality, PAI is capable of revealing the early stages of pathogenesis. Early detection of these pre-disease states is critical when the therapeutic intervention can have the greatest impact. Importantly, by imaging changes in specific aberrations characteristic of disease—such as hemodynamics or ROS generation—the utility of PAI can extend beyond initial diagnosis to monitoring the results of therapeutic intervention. This section covers applications that use both endogenous and exogenous contrast, and examples are highlighted in Table 4.

4.1. Blood and Vasculature

PAI is well suited for vascular imaging because it is optically sensitive to oxygen saturation of hemoglobin at visible and NIR wavelengths, and it can operate at length scales from a few microns to millimeters. PAI can improve upon current methods for vascular imaging, which have various drawbacks including the use of ionizing radiation (CT), requisite contrast agents (pulse-echo US, MRI, CT), minimum flow velocities (speckle variance tracking), and low penetration depths (optical methods).

Angiogenesis refers to the growth of new blood vessel networks and is often correlated to the progression of a tumor. Laufer et al. used a PA scanner and a time-reversal image reconstruction program to create accurate 3D images of angiogenesis *in vivo* at depths of nearly 10 mm and with sub-100 µm spatial resolution [169]. Tumor margins were clearly visualized while showing dynamic

changes such as the recruitment of feeding vessels from surrounding tissue and vessel tortuosity. In addition, by administering the targeted vascular disrupting agent, OXi4503, PA images showed that features of necrosis associated with this agent could be tracked longitudinally. Trebananib is another drug that disrupts angiogenesis. Bohndiek and colleagues showed that PAT could be used to monitor the antiangiogenic efficacy of trebananib by monitoring the tumor hemoglobin concentration and oxygenation in an orthotopic mouse model of ovarian cancer [170].

In 2014, a handheld system was developed that could provide volumetric imaging of spectrally resolved vascular parameters in real time [175]. In a healthy human wrist, the spectral signals from melanin, oxygenated hemoglobin, and deoxygenated hemoglobin were separated and imaged within a few seconds. In mice, favorably low concentrations (10 nM) of the dye ICG were employed to boost contrast and monitor perfusion in the brain, allowing for an overall improvement of sensitivity in deep tissue while using less agent. The application of PAI to functional brain imaging was further developed by Yao et al., who were able to image blood oxygenation, flow, vascular morphology, and O_2 metabolism using PAM [62]. They achieved capillary level resolution while imaging through the intact mouse skull.

Very recently, Li et al. reported the development of a novel PA system, Single-Impulse Panoramic Photoacoustic Computed Tomography (SIP-PACT), which has already been used to image the full mouse body, brain functional connectivity, and track circulating tumor cells in the living vasculature (Figure 8). This scheme improves upon many of the issues encountered with PACT thus far, especially low spatiotemporal resolution beyond 10 mm depths caused by multiplexed signal acquisition, partial spatial sampling, and gaps in acoustic detection space. In its current form, SIP-PACT is designed and optimized for full body imaging of the mouse, combining a ring shaped, 512-element transducer array with multi-source, confocal laser propagation, providing frame rates of 50 Hz and the ability to image vasculature, organs, and sub-organ structures at high spatiotemporal resolution. The team ultimately aims to use it to resolve individual action potentials throughout the brain, which will require even greater advances in spatiotemporal resolution as well as contrast agents sensitive to voltage. It should be understood, however, that full body imaging requires a water bath for coupling, which limits the design at this stage to small animals.

4.2. Reactive Oxygen Species

ROS are highly reactive molecules formed by the reaction of molecular oxygen with electrons and include O_2^-, H_2O_2, $\cdot OH$, and $^1O_2$ (singlet oxygen) [176]. They have been implicated in the etiology of dozens of disease states as well as normal biological functions [177-179]. Because their presence can be linked to both the onset and progression of many diseases, they are powerful targets for monitoring pathogenesis in real-time and measuring therapeutic effects.

In 2014, initial steps were taken to develop real-time probes of pathogenesis in the form of semiconducting π-conjugated polymer nanoparticles (SPNs) [180]. These agents are NIR-active nanoparticles capable of generating bright PA signal. Because of their stability towards ROS, they were conjugated to a cyanine dye (IR775S), sensitive to oxidation by ROS, allowing for spectral differentiation between various ROS. It was shown in murine macrophage cells that activated SPNs could return to their normal state when their environment was no longer saturated with ROS illustrating the real-time monitoring potential for these agents. The SPNs were subsequently proven to highlight regions of increased ROS production in murine models of acute edema. Importantly, these agents could undergo signal evolution following a molecular event, making them activatable. An example of a ROS-sensitive, activatable nanoparticle was demonstrated in 2018—here, a silver-coated gold nanorod was used for simultaneous imaging and treatment of bacterial infection [172]. In this strategy, the PA signal from gold was initially quenched while coated with silver, but was gradually turned on as the silver was etched and released by ROS into sites of infection, exerting bactericidal effects. Activatable probes differentiate themselves from many of the agents used for guided surgeries, which are typically based on accumulation at a target site (relying on the EPR effect) with signal-to-noise ratios proportional to their concentration differences between target and background tissue.

Another activatable probe was recently developed for peroxynitrite. Peroxynitrite (ONOO⁻) is a particularly reactive species, capable of nitrating numerous amino acids, leading to mutation of protein function. It has also shown to play an important role in the immunosuppression of the tumor microenvironment, making it a highly desirable target for understanding the mechanisms that protect tumors from the host immune system and developing effective therapies [181]. Recently, Zhang et al. employed organic semiconducting nanoprobes doped with bulky boranes to enable ratiometric detection of ONOO⁻ in murine tumors with PAI [171]. In short, this strategy allowed the ROS-sensitive component, a NIR-active dye, to shift its absorption upon reaction

with ONOO⁻ (enabling imaging), while the bulky borane prevented reaction with unwanted ROS and maintained a favorable pH in the local environment.
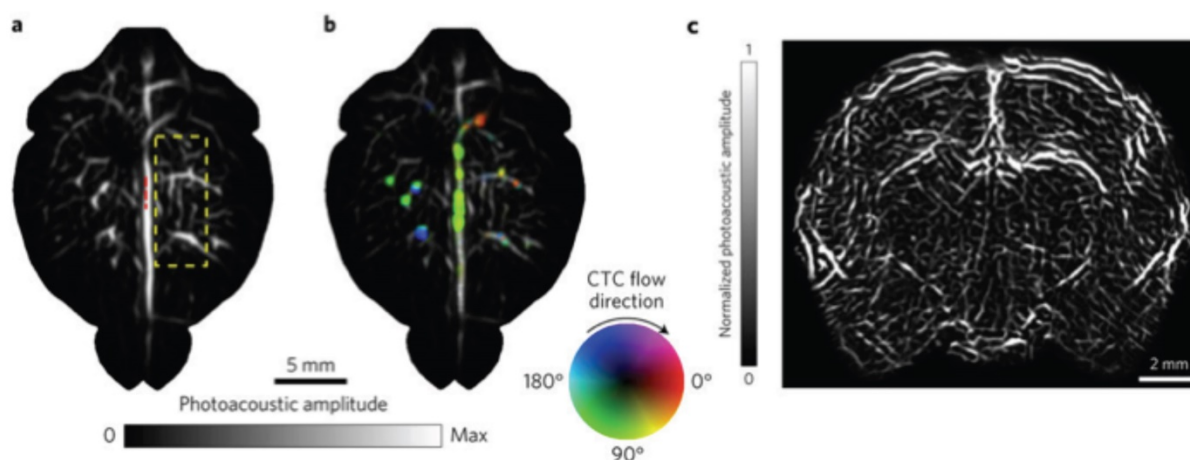
4.3. Lipids

Lipids are essential for many biological functions (energy storage, membrane structure, cell signaling, regulation) but can also perform destructive roles. Unfortunately, existing methods are lacking in their ability to image and quantitatively track lipid molecules in living cells [182]. Cardiovascular health in particular would benefit from such a method. There are currently no reliable techniques to detect vulnerable or unstable arterial plaques prone to rupture (leading to stroke or heart attack) [183]. One of the early studies in biomedical PAI showed that atheromatous (lipid rich) arterial tissue could be distinguished from healthy tissue using wavelengths in the visible range [184]. The characteristic spectra associated with lipids are generated by the overtones of the stretching vibration mode of C-H bonds abundant in their structures [66]. These spectral profiles of lipids are easily distinguished from other vascular constituents, such as collagen, elastin and water [185]. However, visible wavelengths are weakly penetrating and interfere with the absorbance of hemoglobin. Photoacoustic catheter designs can be used to mitigate this issue [186]. Another approach is to use the upper wavelength range of the second NIR window [144] to penetrate tissue more deeply [187], where lipids have peaks around 1200, 1400, and 1700 nm [188].

Table 4. Representative endogenous and exogenous targets used for PA monitoring of therapies and disease states.

Endogenous/Exogenous PA Target	Description	Wavelength (nm)	Image-Guided Outcome	Reference
Hemoglobin	Label-free 3D monitoring of colorectal xenografts in response to vascular disruptor Oxi4503	600, 640, 758	Evaluation of anti-angiogenic therapy	Laufer et al. 2012 [169]
Hemoglobin	Label-free 3D monitoring of orthotopic ovarian tumors following trebananib treatment	757, 797, 837	Evaluation of anti-angiogenic therapy	Bohndiek et al. 2015 [170]
Circulating Tumor Cells	Label-free, real-time monitoring of flow rate and distribution of melanoma CTCs in the mouse brain	680	Tracking of metastatic cancer cell fate for malignancy indication	Li et al. 2017 [118]
Organic Semiconducting Nanoprobes (OSNs)	Boronate-caged boron-dipyrromethane dyes were doped with bulky boranes for imaging peroxynitrite	675	ROS monitoring	Zhang et al. 2017 [171]
Silver-Coated Gold Nanorods	Au/AgNRs were etched by ROS at sites of bacterial infection for Ag ion release and PA imaging	800	ROS monitoring and anti-bacterial treatment	Kim et al. 2018 [172]
Lipid Rich Plaques	Atheromatous lesions of human aortas were spectrally distinguished from healthy areas	970, 1210	Vulnerable plaque identification for atherosclerosis	Allen et al. 2012 [66]
J-Aggregating Nanoparticles	Light-harvesting porphyrins were intercalated with phospholipids to form PA-active nanovesicles sensitive to temperature	680, 824	Monitoring thermal therapy of tumors	Ng et al. 2014 [173]
Oligomerizable Fluorescent Peptide Probes	Furin substrates were linked with an Atto740 fluorophore and cleaved to form aggregated, PA active nanostructures	740	Monitoring proteolytic furin and furin-like activity in tumors	Dragulescu-Andras et al. 2013 [174]

Figure 8. Whole brain vasculature imaging and tracking circulating tumor cells (CTCs) in the mouse brain with SIP-PACT using endogenous contrast (680 nm). (A) Cortical vasculature prior to melanoma cell injection. (B) Vasculature following CTC injection, where flow speed is denoted by hue saturation, encoded radially (where a greater radius designates faster flow speed). (C) Coronal section of the entire rat brain vasculature. Adapted with permission from [118], copyright 2017 Nature Publishing Group.

In 2012, Allen et al. used NIR wavelengths around 1210 nm to image the entire thickness (3 mm) of an atheromatous region of aorta differentiating it from healthy tissue [66]. In addition, they demonstrated the feasibility of imaging through ~3 mm of blood, increasing the ease of use for intravascular implementation. Detection of atheroma in its early stages would allow for therapeutic and lifestyle interventions to prevent the onset of fully staged cardiovascular disease. Similarly, Wang et al. developed a rotational, catheter-based intravascular PA probe for the detection of lipid deposits within plaques of the aorta of rabbits [97]. Their data suggested that imaging of lipids at 1720 nm provided superior contrast to 1210 nm while also requiring lower laser output energy. The imaging speed was limited, however, to about 50 s per frame. To address this limitation, another group constructed a 2-kHz master oscillator power amplifier -pumped, barium nitrite Raman laser [189]. Because of its high repetition rate, pulse-to-pulse stability, and beam quality, this laser was able to image two orders of magnitude faster than prior reports (1.0 s per frame). These developments in intravascular lipid imaging, especially in concert with improvements in
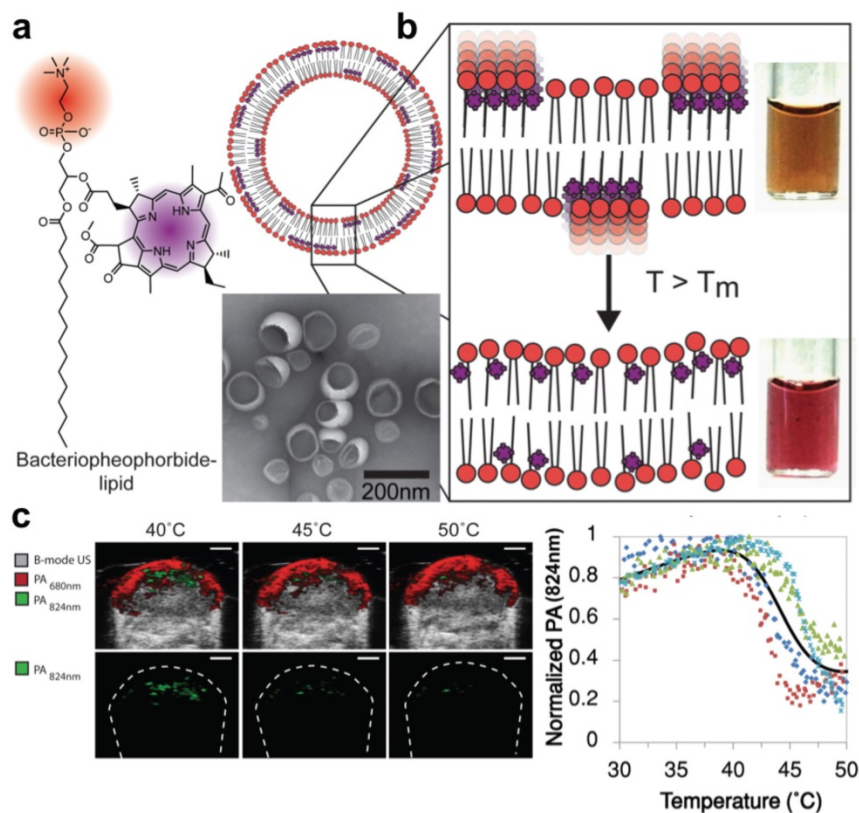
PAE probes, will likely continue to facilitate clinical translation.

4.4. Temperature and pH

Standard thermometers and pH meters can both be used for intravital readings but they cannot obtain precise spatiotemporal data. PAI is fundamentally sensitive to temperature (Equation 1) and can serve as a non-invasive approach for *in vivo* temperature mapping. Additionally, contrast agents for enhanced sensitivity can be used to obtain highly localized measurements of temperature/pH gradients as well as long term temporal monitoring [190]. In comparison to their optical counterparts, PA probes are well-suited for this application because of their deeper penetration depths in tissue and ability to overlap with ultrasound anatomy.

In order to detect temperature changes in tissue following thermal therapy, Ng et al. developed a probe capable of spectral shifting via phase transition [173]. Photosynthetic organisms show a remarkable ability to optimize light absorption using ordered arrangements of pigment molecules within lipid and protein scaffolds. By mimicking this phenomenon with lipid-conjugated, light- absorbing porphyrins, the group assembled aggregates (nanovesicles) with tunable temperature thresholds, allowing for the generation of spatial maps of temperature thresholds to monitor heat therapy with PAI (Figure 9). The exploited mechanism of reversible dye coupling (J-aggregation) can also apply to biological stimuli beyond temperature, such as enzyme and pH detection.

Advancements have also been made in label-free temperature mapping and thermal detection of flow speeds. Typically, it is assumed that a linear correlation exists between temperature and the Grüneisen parameter, and that the temperature is independent from optical fluence [191, 192]. This allows relative temperature mapping based either on calibration measurements or ratiometric changes in PA signals, and avoids quantifying optical tissue parameters [193]. Recently, however, in order to achieve absolute temperature mapping, a multi-illumination PAT method was proposed and simulated that obtains optical

Figure 9. Light-harvesting porphyrin dyes were conjugated within lipid bilayers for measuring temperature via reversible J-aggregation. (A) The structure of a lipid-dye subunit (bacteriopheophorbide-lipid) and representative TEM image are shown. (B) The nanovesicles were composed of 15% Bchl-lipid, 80% host phospholipid and 5% mPEG2000-DPPE. (C) PA-Ultrasound images of a murine tumor xenograft show the PA intensity shift in response to local temperature change by a surrounding water bath, quantified in the last panel where each color is data from one animal (n = 4). Adapted with permission from [173], copyright 2014 American Chemical Society.

parameters, such as the fluence, using multiple illumination sources and an optical diffusion model to quantify temperature directly [194]. This technique achieved relative errors between 10.6-15.7%, but has not yet been applied beyond simulation. Another interesting temperature- based PA technique was demonstrated by Liu et al., who developed a flowmetry method based on OR-PAM that uses a pulsed light source for both "thermal tagging" and photoacoustic excitation [195]. It leverages the correlation between the Grüneisen parameter and local temperature to measure thermal dynamics and flow speed of homogenous or nonhomogeneous media. The authors were able to measure flow speeds (e.g. 2.55, 0.96, 0.99 mm/s) in the microvasculature of a mouse ear based on thermal fluctuations.

Aberrations in physiological parameters such as pH are associated with a number of conditions and diseases, including ischemia, inflammation, cancer, chronic obstructive pulmonary disease, and kidney failure [196]. Existing methods for *in vivo* pH detection rely primarily on dye fluorescence, which is hindered by light scattering, cytosolic leakage, and varying photostabilities [197]. In 2016, Miao et al. developed an activatable probe for the detection of pH, combining a semiconducting oligomer matrix (for PA signal) with a boron-dipyrromethene dye (for pH indication and PA enhancement) [198]. The dye backbone contained hydroxyl groups allowing for protonation upon exposure to acids, endowing the probe with sensitivity to pH. The researchers showed that in mice, a dose of 25 µg was sufficient for real time, ratiometric mapping of pH in tumors.
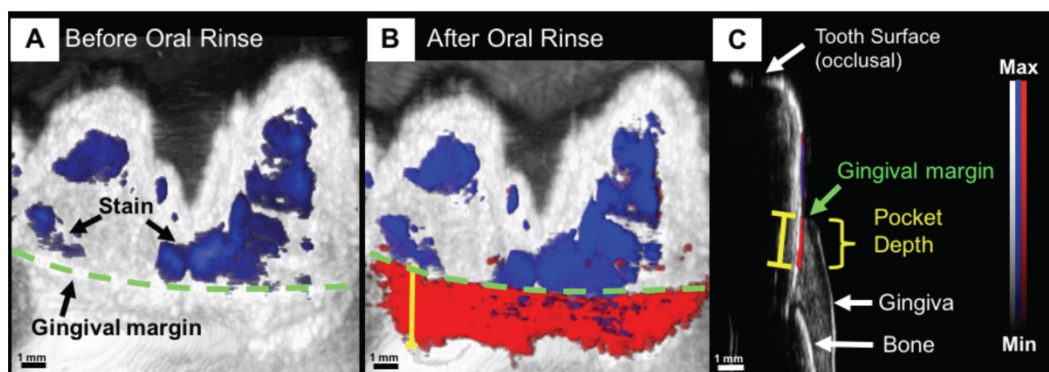
In 2013, PAI was used to monitor and image enzyme activity. Dragulescu-Andrasi et al. targeted the protease, furin, which plays a role in tumor regulation and normal cell function [174]. They devised an enzyme-sensitive oligomerizable reactive PA probe consisting of a peptide substrate, two pro-reactive moieties, and the NIR active PA molecule Atto740, sensitive even in deep tissue. The ability to image furin activity was shown in mice, and the probe could be theoretically adapted to interrogate other enzymes of interest. In another enzyme-responsive system, Chen et. al developed a micellar probe combining indocyanine green with an alkaline phosphatase-specific peptide for combination PAI and PTT. Here, the probes had prolonged circulation/ tumor accumulation and could convert to a nanofiber morphology once the peptides were phosphorylated by alkaline phosphatase in the tumor microenvironment [199]. In this form, the probes had 25-fold higher tumor uptake than free indocyanine green at 4 h after injection, while facilitating PTT (0.8 W/cm^2, 5 min)

with high therapeutic efficacy. Enzyme-sensitive contrast agents hold significant biological interest but PA applications are still in their early stages. It is likely that strategies from other imaging modalities can be borrowed; for example, FRET-based mechanisms, responsive hydrogels, and assembly/ disassembly of micelles [200]. However, some challenges include honing the specificity of engineered probes for their target enzymes (especially against members of the same enzyme family, e.g. matrix metalloproteinases), and choosing feasible targets that do not require deep tissue penetration.

5. Outlook and Future Developments

The applications and capabilities of photoacoustic technology are growing at a rapid pace. The development of novel PA systems such as SIP-PACT (Section 4.1), forward-viewing PAE (Section 2.1), and handheld PAM (Section 1.3) are promising examples of hardware innovations [54, 60, 118]. These advances are pushing the state of the art toward finer resolutions and new areas of application. It is feasible that the spatial resolutions of PAI will continue to improve as transducer elements become more affordable and image reconstruction algorithms are refined to address problems such as the heterogeneity of the speed of sound through various tissues [201]. Additionally, lower cost systems with excitation sources such as laser diodes [202] and light emitting diodes (LEDs) [203, 204], which are more stable, may increase the accessibility of PAI for researchers and clinicians alike. Furthermore, contrast agents with absorbance maxima at longer wavelengths in the second optical window will be increasingly developed to improve the depths at which PAI is effective. This will likely mirror the recent progress in fluorescence imaging, where new NIR-II fluorophores have been pushing the field forward [18, 205, 206]. Analogous PA materials should become more common as the chemistry develops. Fortunately, PA systems do not need to implement expensive, high quantum efficiency detectors (InGaAs or HgCdTe) that are required for fluorescence imaging in the second optical window [19]. Instead, however, they must implement longer wavelength lasers—e.g., the commercial Vevo LAZR-X includes a 1200-2000 nm laser in addition to a 680-970 nm source (though this combination excludes the 1000-1200 nm range) [18, 79]. In the short-term, we believe that biodegradable contrast agents, small molecule dyes (especially those with existing FDA approval), and techniques that do not require intravenous injection will have the shortest paths to the clinic.

Figure 10. Non-invasive and precise measurement of porcine periodontal pocket depths using PAI. (A) PA/Ultrasound image of the gum line (green) and tooth with stains (blue) at 680 nm, prior to oral rinse of contrast agent. (B) Image following oral rinse with contrast agent, revealing the pocket (red) under the gum line. (C) Sagittal view of a 3D PA scan of the tooth, distinguishing hard and soft tissue, and revealing the PA signal from the contrast agent beginning at the gingival margin and extending through the pocket depth [209].

As the technology itself continues to develop, so does the application space. Work is underway by numerous groups on alternative transducer designs for specialized applications, including through-needle imaging for guided surgery [207], PA-guided surgical drilling [96], and human finger joint imaging [208]. "Wearable" PA devices are another example. The concept was recently demonstrated for dental imaging, specifically, non-invasive periodontal pocket depth measurements for early gum disease diagnosis (Figure 10). Here, a contrast agent derived from food-grade cuttlefish ink (rich in melanin nanoparticles) was used with PAT to image the pockets between gum and teeth, showing potential for a PA mouthpiece device [209, 210].

It is also worth recognizing progress in Magneto-Acoustic Imaging (MAI), a technique similar to PAI, but in which magnetic contrast agents are used to label tissue, whereafter a pulsed magnetic field is used to induce motion of the agents within the tissue, detectable by ultrasound [211]. Such a technique would circumvent the need for optical penetration. Proof-of-concept has been demonstrated in cells and tissue phantoms and MAI remains in its early stages, but may see progress in the near future that parallels the recent growth of photoacoustics [212].

PAI will likely never become as widespread as MRI or CT, but it is highly complementary to ultrasound, already one of the most widely available imaging tools in medicine. While ultrasound generates anatomical images, PAI adds to this the molecular and functional contrast that is normally associated with optical imaging techniques. The clinical appeal of this combination will be a driving force for the continued growth of photoacoustic imaging.

Abbreviations

APTT: activated partial thromboplastin time; AR-PAM: acoustic resolution-photoacoustic microscopy; AuNR: gold nanorod; CT: computed tomo-graphy; CTC: circulating tumor cell; CW: continuous wave; EPR: enhanced permeability and retention; FDA: food and drug administration; GI: gastrointestinal; HIFU: high intensity focused ultrasound; ICG: indocyanine green; IONPs: iron oxide nanoparticles; IV: intravascular; LCST: lower critical saturation temperature; LEDs: light emitting diodes; MAI: magnetic acoustic imaging; MEMS: micro-electro-mechanical systems; MRI: magnetic resonance imaging; MSOT: multispectral optoacoustic tomography; NIR: near infrared; OR-PAM: optical resolution-photoacoustic microscopy; PA: photoacoustic; PACT: photoacoustic computed tomography; PAE: photoacoustic endoscopy; PAI: photoacoustic imaging; PAM: photoacoustic microscopy; PAT: photoacoustic tomography; PDT: photodynamic therapy; PEG: polyethylene glycol; PET: positron emission tomography; PFC: perfluorocarbon; PNIPAM: poly(N-isospropylacrylamide); PTT: photothermal therapy; ROS: reactive oxygen species; SIP-PACT: single-impulse panoramic photoacoustic computed tomography; SLN: sentinel lymph node; SO_2: oxygen saturation; sPA: spectroscopic photoacoustic imaging; SPNs: semiconducting polymer nanoparticles; TMDCs: transition metal dichalcogenides.

Acknowledgements

Competing Interests

The authors have declared that no competing interest exists.

References

1. Ntziachristos V, Razansky D. Molecular Imaging by Means of Multispectral Optoacoustic Tomography (MSOT). Chemical Reviews. 2010; 110: 2783-94.
2. Kim C, Favazza C, Wang LV. In vivo photoacoustic tomography of chemicals: high-resolution functional and molecular optical imaging at new depths. Chemical reviews. 2010; 110: 2756-82.

3. Wang LV, Hu S. Photoacoustic Tomography: In Vivo Imaging from Organelles to Organs. Science (New York, Ny). 2012; 335: 1458-62.
4. Xia J, Yao J, Wang LV. Photoacoustic tomography: principles and advances. Electromagnetic waves (Cambridge, Mass). 2014; 147: 1-22.
5. Wang LV, Yao J. A practical guide to photoacoustic tomography in the life sciences. Nat Meth. 2016; 13: 627-38.
6. Beard P. Biomedical photoacoustic imaging. Interface Focus. 2011; 1: 602-31.
7. Luke GP, Yeager D, Emelianov SY. Biomedical applications of photoacoustic imaging with exogenous contrast agents. Annals of biomedical engineering. 2012; 40: 422-37.
8. Weber J, Beard PC, Bohndiek SE. Contrast agents for molecular photoacoustic imaging. Nat Meth. 2016; 13: 639-50.
9. Nie L, Chen X. Structural and functional photoacoustic molecular tomography aided by emerging contrast agents. Chemical Society Reviews. 2014; 43: 7132-70.
10. Fu Q, Zhu R, Song J, Yang H, Chen X. Photoacoustic Imaging: Contrast Agents and Their Biomedical Applications. Advanced Materials. 2018; 0: 1805875.
11. Huang X, Song J, Yung BC, Huang X, Xiong Y, Chen X. Ratiometric optical nanoprobes enable accurate molecular detection and imaging. Chemical Society Reviews. 2018; 47: 2873-920.
12. Miao Q, Pu K. Emerging Designs of Activatable Photoacoustic Probes for Molecular Imaging. Bioconjugate Chemistry. 2016; 27: 2808-23.
13. Li W, Chen X. Gold nanoparticles for photoacoustic imaging. Nanomedicine. 2015; 10: 299-320.
14. Manohar S, Ungureanu C, Van Leeuwen TG. Gold nanorods as molecular contrast agents in photoacoustic imaging: the promises and the caveats. Contrast Media & Molecular Imaging. 2011; 6: 389-400.
15. Cho EC, Glaus C, Chen J, Welch MJ, Xia Y. Inorganic nanoparticle-based contrast agents for molecular imaging. Trends in molecular medicine. 2010; 16: 561-73.
16. Lin L-S, Song J, Yang H-H, Chen X. Yolk–Shell Nanostructures: Design, Synthesis, and Biomedical Applications. Advanced Materials. 2018; 30: 1704639.
17. Liu Y, Bhattarai P, Dai Z, Chen X. Photothermal therapy and photoacoustic imaging via nanotheranostics in fighting cancer. Chemical Society Reviews. 2019.
18. Huang K, Zhang Y, Lin J, Huang P. Nanomaterials for photoacoustic imaging in the second near-infrared window. Biomaterials science. 2018.
19. Jiang Y, Pu K. Molecular Fluorescence and Photoacoustic Imaging in the Second Near-Infrared Optical Window Using Organic Contrast Agents. Advanced Biosystems. 2018; 2: 1700262.
20. Jiang Y, Pu K. Advanced photoacoustic imaging applications of near-infrared absorbing organic nanoparticles. Small. 2017; 13: 1700710.
21. Li K, Liu B. Polymer-encapsulated organic nanoparticles for fluorescence and photoacoustic imaging. Chemical Society Reviews. 2014; 43: 6570-97.
22. Li J, Pu K. Development of organic semiconducting materials for deep-tissue optical imaging, phototherapy and photoactivation. Chemical Society Reviews. 2019; 48: 38-71.
23. Jiang Y, Pu K. Multimodal Biophotonics of Semiconducting Polymer Nanoparticles. Accounts of Chemical Research. 2018; 51: 1840-9.
24. Hu S, Wang LV. Neurovascular photoacoustic tomography. Frontiers in neuroenergetics. 2010; 2: 10.
25. Wang D, Wu Y, Xia J. Review on photoacoustic imaging of the brain using nanoprobes. Neurophotonics. 2016; 3: 010901.
26. Hu S, Wang LV. Photoacoustic imaging and characterization of the microvasculature. Journal of biomedical optics. 2010; 15: 011101.
27. Mallidi S, Luke GP, Emelianov S. Photoacoustic imaging in cancer detection, diagnosis, and treatment guidance. Trends in biotechnology. 2011; 29: 213-21.
28. Xia J, Kim C, Lovell JF. Opportunities for Photoacoustic-Guided Drug Delivery. Curr Drug Targets. 2015; 16: 571-81.
29. Bell AG. The photophone. Journal of the Franklin Institute. 1880; 110: 237-48.
30. Bell AG. The Production of Sound by Radiant Energy. Science. 1881; 2: 242-53.
31. Rosencwaig A, Gersho A. Theory of the photoacoustic effect with solids. Journal of Applied Physics. 1976; 47: 64-9.
32. Bowen T. Radiation-induced thermoacoustic imaging. Google Patents; 1983.
33. Kruger RA. Photoacoustic ultrasound. Medical Physics. 1994; 21: 127-31.
34. Kruger RA, Liu P, Fang YR, Appledorn CR. Photoacoustic ultrasound (PAUS)—Reconstruction tomography. Medical Physics. 1995; 22: 1605-9.
35. Hoelen C, De Mul F, Pongers R, Dekker A. Three-dimensional photoacoustic imaging of blood vessels in tissue. Optics letters. 1998; 23: 648-50.
36. Wang LV, Zhao X, Sun H, Ku G. Microwave-induced acoustic imaging of biological tissues. Review of scientific instruments. 1999; 70: 3744-8.
37. Zackrisson S, van de Ven S, Gambhir S. Light in and sound out: emerging translational strategies for photoacoustic imaging. Cancer research. 2014; 74: 979-1004.
38. Sordillo LA, Pu Y, Pratavieira S, Budansky Y, Alfano RR. Deep optical imaging of tissue using the second and third near-infrared spectral windows. Journal of Biomedical Optics. 2014; 19: 056004-.
39. Frangioni JV. In vivo near-infrared fluorescence imaging. Current opinion in chemical biology. 2003; 7: 626-34.
40. Cox B, Laufer JG, Arridge SR, Beard PC. Quantitative spectroscopic photoacoustic imaging: a review. Journal of Biomedical Optics. 2012; 17: 0612021-06120222.
41. Maslov K, Wang LV. Photoacoustic imaging of biological tissue with intensity-modulated continuous-wave laser. Journal of biomedical optics. 2008; 13: 024006--5.
42. Wang X, Pang Y, Ku G, Xie X, Stoica G, Wang LV. Noninvasive laser-induced photoacoustic tomography for structural and functional in vivo imaging of the brain. Nature biotechnology. 2003; 21: 803-6.
43. Lashkari B, Mandelis A. Comparison between pulsed laser and frequency-domain photoacoustic modalities: signal-to-noise ratio, contrast, resolution, and maximum depth detectivity. Review of Scientific Instruments. 2011; 82: 094903.
44. Xu M, Wang LV. Photoacoustic imaging in biomedicine. Review of scientific instruments. 2006; 77: 041101.
45. Pramanik M, Wang LV. Thermoacoustic and photoacoustic sensing of temperature. Journal of biomedical optics. 2009; 14: 054024--7.
46. Wang LV. Multiscale photoacoustic microscopy and computed tomography. Nature photonics. 2009; 3: 503-9.
47. Zhang C, Wang Y. Comparison of Various Imaging Modes for Photoacoustic Tomography. Springer Berlin Heidelberg; 2009: 121-4.
48. Zhang HF, Maslov K, Stoica G, Wang LV. Functional photoacoustic microscopy for high-resolution and noninvasive in vivo imaging. Nature Biotechnology. 2006; 24: 848.
49. Hu S, Maslov K, Wang LV. Second-generation optical-resolution photoacoustic microscopy with improved sensitivity and speed. Optics Letters. 2011; 36: 1134.
50. Zhang C, Maslov KI, Hu S, Wang LV, Chen R, Zhou Q, et al. Reflection-mode submicron-resolution in vivo photoacoustic microscopy. SPIE; 2012: 4.
51. Lan B, Liu W, Wang Y-c, Shi J, Li Y, Xu S, et al. High-speed widefield photoacoustic microscopy of small-animal hemodynamics. Biomedical Optics Express. 2018; 9: 4689-701.
52. Lan B, Liu W, Yao J. High-speed wide-field photoacoustic microscopy. Clinical and Translational Biophotonics: Optical Society of America; 2018: JTu3A. 68.
53. Favazza CP, Jassim O, Cornelius LA, Wang LV. In vivo photoacoustic microscopy of human cutaneous microvasculature and a nevus. Journal of Biomedical Optics. 2011; 16: 016015.
54. Park K, Kim JY, Lee C, Jeon S, Lim G, Kim C. Handheld Photoacoustic Microscopy Probe. Scientific Reports. 2017; 7: 13359.
55. Xu M, Wang LV. Universal back-projection algorithm for photoacoustic computed tomography. Physical Review E. 2005; 71: 016706.
56. Schellenberg MW, Hunt HK. Hand-held optoacoustic imaging: A review. Photoacoustics. 2018; 11: 14-27.
57. Yang J-M, Maslov K, Yang H-C, Zhou Q, Shung KK, Wang LV. Photoacoustic endoscopy. Optics letters. 2009; 34: 1591-3.
58. Yang J-M, Favazza C, Chen R, Yao J, Cai X, Maslov K, et al. Simultaneous functional photoacoustic and ultrasonic endoscopy of internal organs in vivo. Nature medicine. 2012; 18: 1297-302.
59. Nikoozadeh A, Choe JW, Kothapalli S-R, Moini A, Sanjani SS, Kamaya A, et al. Photoacoustic imaging using a 9F microLinear CMUT ICE catheter. Ultrasonics Symposium (IUS), 2012 IEEE International: IEEE; 2012: 24-7.
60. Ansari R, Zhang EZ, Desjardins AE, Beard PC. All-optical forward-viewing photoacoustic probe for high-resolution 3D endoscopy. Light: Science & Applications. 2018; 7: 75.
61. Zhang HF, Maslov K, Wang LV. In vivo imaging of subcutaneous structures using functional photoacoustic microscopy. Nature protocols. 2007; 2: 797-804.
62. Yao J, Wang L, Yang J-M, Maslov KI, Wong TTW, Li L, et al. High-speed label-free functional photoacoustic microscopy of mouse brain in action. Nat Meth. 2015; 12: 407-10.
63. Wang LV, Wu H-i. Biomedical optics: principles and imaging: John Wiley & Sons; 2012.
64. Zhang HF, Maslov K, Sivaramakrishnan M, Stoica G, Wang LV. Imaging of hemoglobin oxygen saturation variations in single vessels in vivo using photoacoustic microscopy. Applied physics letters. 2007; 90: 053901.
65. Oh J-T, Li M-L, Zhang HF, Maslov K, Stoica G, Wang LV. Three-dimensional imaging of skin melanoma in vivo by dual-wavelength photoacoustic microscopy. Journal of biomedical optics. 2006; 11: 034032--4.
66. Allen TJ, Hall A, Dhillon AP, Owen JS, Beard PC. Spectroscopic photoacoustic imaging of lipid-rich plaques in the human aorta in the 740 to 1400 nm wavelength range. Journal of biomedical optics. 2012; 17: 0612091-06120910.
67. Lemaster JE, Jokerst JV. What is new in nanoparticle-based photoacoustic imaging? Wiley Interdisciplinary Reviews: Nanomedicine and Nanobiotechnology. 2017; 9.
68. Thakor AS, Jokerst JV, Ghanouni P, Campbell JL, Mittra E, Gambhir SS. Clinically approved nanoparticle imaging agents. Journal of Nuclear Medicine. 2016; 57: 1833-7.
69. Albanese A, Tang PS, Chan WCW. The Effect of Nanoparticle Size, Shape, and Surface Chemistry on Biological Systems. Annual Review of Biomedical Engineering. 2012; 14: 1-16.
70. Sun T, Zhang YS, Pang B, Hyun DC, Yang M, Xia Y. Engineered Nanoparticles for Drug Delivery in Cancer Therapy. Angewandte Chemie International Edition. 2014; 53: 12320-64.
71. Jain PK, Lee KS, El-Sayed IH, El-Sayed MA. Calculated Absorption and Scattering Properties of Gold Nanoparticles of Different Size, Shape, and Composition: Applications in Biological Imaging and Biomedicine. The Journal of Physical Chemistry B. 2006; 110: 7238-48.
72. Feis A, Gellini C, Salvi PR, Becucci M. Photoacoustic excitation profiles of gold nanoparticles. Photoacoustics. 2014; 2: 47-53.

73. Zhou Y, Wang D, Zhang Y, Chitgupi U, Geng J, Wang Y, et al. A Phosphorus Phthalocyanine Formulation with Intense Absorbance at 1000 nm for Deep Optical Imaging. Theranostics. 2016; 6: 688-97.

74. Salehi HS, Kumavor PD, Li H, Alqasemi U, Wang T, Xu C, et al. Design of optimal light delivery system for co-registered transvaginal ultrasound and photoacoustic imaging of ovarian tissue. Photoacoustics. 2015; 3: 114-22.

75. El-Gohary SH, Metwally MK, Eom S, Jeon SH, Byun KM, Kim T-S. Design study on photoacoustic probe to detect prostate cancer using 3D Monte Carlo simulation and finite element method. Biomedical Engineering Letters. 2014; 4: 250-7.

76. Bell MAL, Kuo NP, Song DY, Kang JU, Boctor EM. In vivo visualization of prostate brachytherapy seeds with photoacoustic imaging. Journal of biomedical optics. 2014; 19: 126011-.

77. Yang J-M, Favazza CP, Yao J, Chen R, Zhou Q, Shung KK, et al. Three-dimensional photoacoustic and ultrasonic endoscopic imaging of two rabbit esophagi. SPIE BiOS: International Society for Optics and Photonics; 2015: 932334--8.

78. Smith AM, Mancini MC, Nie S. Bioimaging: second window for in vivo imaging. Nature nanotechnology. 2009; 4: 710-1.

79. Jiang Y, Upputuri PK, Xie C, Lyu Y, Zhang L, Xiong Q, et al. Broadband Absorbing Semiconducting Polymer Nanoparticles for Photoacoustic Imaging in Second Near-Infrared Window. Nano Letters. 2017; 17: 4964-9.

80. Welsher K, Liu Z, Sherlock SP, Robinson JT, Chen Z, Daranciang D, et al. A route to brightly fluorescent carbon nanotubes for near-infrared imaging in mice. Nature nanotechnology. 2009; 4: 773-80.

81. Park JE, Kim M, Hwang JH, Nam JM. Golden Opportunities: Plasmonic Gold Nanostructures for Biomedical Applications based on the Second Near-Infrared Window. Small Methods. 2017; 1: 1600032.

82. Ku G, Zhou M, Song S, Huang Q, Hazle J, Li C. Copper sulfide nanoparticles as a new class of photoacoustic contrast agent for deep tissue imaging at 1064 nm. Acs Nano. 2012; 6: 7489-96.

83. Homan KA, Souza M, Truby R, Luke GP, Green C, Vreeland E, et al. Silver nanoplate contrast agents for in vivo molecular photoacoustic imaging. ACS nano. 2012; 6: 641-50.

84. Steeg PS, Theodorescu D. Metastasis: a therapeutic target for cancer. Nature clinical practice Oncology. 2008; 5: 206-19.

85. Grootendorst D, Jose J, Wouters M, van Boven H, Van der Hage J, Van Leeuwen T, et al. First experiences of photoacoustic imaging for detection of melanoma metastases in resected human lymph nodes. Lasers in surgery and medicine. 2012; 44: 541-9.

86. Langhout GC, Grootendorst DJ, Nieweg OE, Wouters MWJM, Hage JAvd, Jose J, et al. Detection of melanoma metastases in resected human lymph nodes by noninvasive multispectral photoacoustic imaging. Journal of Biomedical Imaging. 2014; 2014: 5.

87. Luke GP, Emelianov SY. Label-free Detection of Lymph Node Metastases with US-guided Functional Photoacoustic Imaging. Radiology. 2015; 277: 435-42.

88. Wang Y, Hu S, Maslov K, Zhang Y, Xia Y, Wang LV. In vivo integrated photoacoustic and confocal microscopy of hemoglobin oxygen saturation and oxygen partial pressure. Optics letters. 2011; 36: 1029-31.

89. Ning B, Kennedy MJ, Dixon AJ, Sun N, Cao R, Soetikno BT, et al. Simultaneous photoacoustic microscopy of microvascular anatomy, oxygen saturation, and blood flow. Optics letters. 2015; 40: 910-3.

90. Xi L, Grobmyer SR, Wu L, Chen R, Zhou G, Gutwein LG, et al. Evaluation of breast tumor margins in vivo with intraoperative photoacoustic imaging. Optics express. 2012; 20: 8726-31.

91. Neuschmelting V, Burton NC, Lockau H, Urich A, Harmsen S, Ntziachristos V, et al. Performance of a Multispectral Optoacoustic Tomography (MSOT) System equipped with 2D vs. 3D Handheld Probes for Potential Clinical Translation. Photoacoustics. 2016; 4: 1-10.

92. Neuschmelting V, Lockau H, Ntziachristos V, Grimm J, Kircher MF. Lymph Node Micrometastases and In-Transit Metastases from Melanoma: In Vivo Detection with Multispectral Optoacoustic Imaging in a Mouse Model. Radiology. 2016; 280: 137-50.

93. Horiguchi A, Tsujita K, Irisawa K, Kasamatsu T, Hirota K, Kawaguchi M, et al. A pilot study of photoacoustic imaging system for improved real-time visualization of neurovascular bundle during radical prostatectomy. The Prostate. 2016; 76: 307-15.

94. Moradi H, Tang S, Salcudean SE. Toward Intra-Operative Prostate Photoacoustic Imaging: Configuration Evaluation and Implementation Using the da Vinci Research Kit. IEEE Transactions on Medical Imaging. 2019; 38: 57-68.

95. Gandhi N, Allard M, Kim S, Kazanzides P, Lediju Bell MA. Photoacoustic-based approach to surgical guidance performed with and without a da Vinci robot. Journal of Biomedical Optics. 2017; 22: 121606.

96. Eddins B, Bell MAL. Design of a multifiber light delivery system for photoacoustic-guided surgery. Journal of biomedical optics. 2017; 22: 041011.

97. Wang B, Karpiouk A, Yeager D, Amirian J, Litovsky S, Smalling R, et al. Intravascular photoacoustic imaging of lipid in atherosclerotic plaques in the presence of luminal blood. Optics letters. 2012; 37: 1244-6.

98. Wang B, Su JL, Karpiouk AB, Sokolov KV, Smalling RW, Emelianov SY. Intravascular photoacoustic imaging. IEEE Journal of selected topics in Quantum Electronics. 2010; 16: 588-99.

99. Jansen K, Van Der Steen AF, van Beusekom HM, Oosterhuis JW, van Soest G. Intravascular photoacoustic imaging of human coronary atherosclerosis. Optics letters. 2011; 36: 597-9.

100. Wu M, Springeling G, Lovrak M, Mastik F, Iskander-Rizk S, Wang T, et al. Real-time volumetric lipid imaging in vivo by intravascular photoacoustics at 20 frames per second. Biomedical optics express. 2017; 8: 943-53.

101. Yang J-M, Li C, Chen R, Zhou Q, Shung KK, Wang LV. Catheter-based photoacoustic endoscope. Journal of biomedical optics. 2014; 19: 066001.

102. Iwashita T, Nakai Y, Lee JG, Park DH, Muthusamy VR, Chang KJ. Newly-developed, forward-viewing echoendoscope: A comparative pilot study to the standard echoendoscope in the imaging of abdominal organs and feasibility of endoscopic ultrasound-guided interventions. Journal of Gastroenterology and Hepatology. 2012; 27: 362-7.

103. Dong B, Chen S, Zhang Z, Sun C, Zhang HF. Photoacoustic probe using a microring resonator ultrasonic sensor for endoscopic applications. Optics letters. 2014; 39: 4372-5.

104. Wilson KE, Bachawal SV, Abou-Elkacem L, Jensen K, Machtaler S, Tian L, et al. Spectroscopic Photoacoustic Molecular Imaging of Breast Cancer using a B7-H3-targeted ICG Contrast Agent. Theranostics. 2017; 7: 1463-76.

105. Jokerst JV, Cole AJ, Van de Sompel D, Gambhir SS. Gold nanorods for ovarian cancer detection with photoacoustic imaging and resection guidance via Raman imaging in living mice. ACS nano. 2012; 6: 10366-77.

106. Grootendorst DJ, Jose J, Fratila RM, Visscher M, Velders AH, Ten Haken B, et al. Evaluation of superparamagnetic iron oxide nanoparticles (Endorem®) as a photoacoustic contrast agent for intra-operative nodal staging. Contrast media & molecular imaging. 2013; 8: 83-91.

107. Ray A, Wang X, Lee Y-EK, Hah HJ, Kim G, Chen T, et al. Targeted blue nanoparticles as photoacoustic contrast agent for brain tumor delineation. Nano research. 2011; 4: 1163-73.

108. Guan T, Shang W, Li H, Yang X, Fang C, Tian J, et al. From Detection to Resection: Photoacoustic Tomography and Surgery Guidance with Indocyanine Green Loaded Gold Nanorod@liposome Core–Shell Nanoparticles in Liver Cancer. Bioconjugate Chemistry. 2017; 28: 1221-8.

109. Maeda A, Bu J, Chen J, Zheng G, DaCosta RS. Dual in vivo Photoacoustic and Fluorescence Imaging of HER2 Expression in Breast Tumors for Diagnosis, Margin Assessment, and Surgical Guidance. Molecular Imaging. 2015; 14: 7290.2014.00043.

110. Kircher MF, de la Zerda A, Jokerst JV, Zavaleta CL, Kempen PJ, Mittra E, et al. A Brain Tumor Molecular Imaging Strategy Using A New Triple-Modality MRI-Photoacoustic-Raman Nanoparticle. Nature medicine. 2012; 18: 829-34.

111. Harisinghani MG, Barentsz J, Hahn PF, Deserno WM, Tabatabaei S, van de Kaa CH, et al. Noninvasive Detection of Clinically Occult Lymph-Node Metastases in Prostate Cancer. New England Journal of Medicine. 2003; 348: 2491-9.

112. Xi L, Zhou G, Gao N, Yang L, Gonzalo DA, Hughes SJ, et al. Photoacoustic and Fluorescence Image-Guided Surgery Using a Multifunctional Targeted Nanoprobe. Annals of surgical oncology. 2014; 21: 1602-9.

113. Shakiba M, Ng KK, Huynh E, Chan H, Charron DM, Chen J, et al. Stable J-aggregation enabled dual photoacoustic and fluorescence nanoparticles for intraoperative cancer imaging. Nanoscale. 2016; 8: 12618-25.

114. Mallidi S, Larson T, Tam J, Joshi PP, Karpiouk A, Sokolov K, et al. Multiwavelength photoacoustic imaging and plasmon resonance coupling of gold nanoparticles for selective detection of cancer. Nano letters. 2009; 9: 2825-31.

115. Sethuraman S, Amirian JH, Litovsky SH, Smalling RW, Emelianov SY. Spectroscopic intravascular photoacoustic imaging to differentiate atherosclerotic plaques. Optics express. 2008; 16: 3362-7.

116. Afshar-Oromieh A, Malcher A, Eder M, Eisenhut M, Linhart H, Hadaschik B, et al. PET imaging with a [68 Ga] gallium-labelled PSMA ligand for the diagnosis of prostate cancer: biodistribution in humans and first evaluation of tumour lesions. European journal of nuclear medicine and molecular imaging. 2013; 40: 486-95.

117. Yang K, Wan J, Zhang S, Zhang Y, Lee S-T, Liu Z. In vivo pharmacokinetics, long-term biodistribution, and toxicology of PEGylated graphene in mice. ACS nano. 2010; 5: 516-22.

118. Li L, Zhu L, Ma C, Lin L, Yao J, Wang L, et al. Single-impulse panoramic photoacoustic computed tomography of small-animal whole-body dynamics at high spatiotemporal resolution. Nature Biomedical Engineering. 2017; 1: 0071.

119. Lyu Y, Fang Y, Miao Q, Zhen X, Ding D, Pu K. Intraparticle Molecular Orbital Engineering of Semiconducting Polymer Nanoparticles as Amplified Theranostics for in Vivo Photoacoustic Imaging and Photothermal Therapy. ACS Nano. 2016; 10: 4472-81.

120. Zhang Y, Jeon M, Rich LJ, Hong H, Geng J, Zhang Y, et al. Non-invasive multimodal functional imaging of the intestine with frozen micellar naphthalocyanines. Nature nanotechnology. 2014; 9: 631-8.

121. Liu T, Wang C, Cui W, Gong H, Liang C, Shi X, et al. Combined photothermal and photodynamic therapy delivered by PEGylated MoS2 nanosheets. Nanoscale. 2014; 6: 11219-25.

122. Tian G, Zhang X, Zheng X, Yin W, Ruan L, Liu X, et al. Multifunctional RbxWO3 Nanorods for Simultaneous Combined Chemo-photothermal Therapy and Photoacoustic/CT Imaging. Small. 2014; 10: 4160-70.

123. Moon GD, Choi S-W, Cai X, Li W, Cho EC, Jeong U, et al. A New Theranostic System Based on Gold Nanocages and Phase-Change Materials with Unique Features for Photoacoustic Imaging and Controlled Release. Journal of the American Chemical Society. 2011; 133: 4762-5.

124. Manivasagan P, Bharathiraja S, Bui NQ, Jang B, Oh Y-O, Lim IG, et al. Doxorubicin-loaded fucoidan capped gold nanoparticles for drug delivery

and photoacoustic imaging. International journal of biological macromolecules. 2016; 91: 578-88.

125. Zhong J, Yang S, Wen L, Xing D. Imaging-guided photoacoustic drug release and synergistic chemo-photoacoustic therapy with paclitaxel-containing nanoparticles. Journal of Controlled Release. 2016; 226: 77-87.

126. Ho I-T, Sessler JL, Gambhir SS, Jokerst JV. Parts per billion detection of uranium with a porphyrinoid-containing nanoparticle and in vivo photoacoustic imaging. Analyst. 2015; 140: 3731-7.

127. Cash KJ, Li C, Xia J, Wang LV, Clark HA. Optical Drug Monitoring: Photoacoustic Imaging of Nanosensors to Monitor Therapeutic Lithium in Vivo. ACS Nano. 2015; 9: 1692-8.

128. Jeevarathinam AS, Pai N, Huang K, Hariri A, Wang J, Bai Y, et al. A cellulose-based photoacoustic sensor to measure heparin concentration and activity in human blood samples. Biosensors and Bioelectronics. 2019; 126: 831-7.

129. Wilson K, Homan K, Emelianov S. Biomedical photoacoustics beyond thermal expansion using triggered nanodroplet vaporization for contrast-enhanced imaging. Nature Communications. 2012; 3: 618.

130. Lovell JF, Jin CS, Huynh E, Jin H, Kim C, Rubinstein JL, et al. Porphysome nanovesicles generated by porphyrin bilayers for use as multimodal biophotonic contrast agents. Nat Mater. 2011; 10: 324-32.

131. Huynh E, Jin CS, Wilson BC, Zheng G. Aggregate Enhanced Trimodal Porphyrin Shell Microbubbles for Ultrasound, Photoacoustic, and Fluorescence Imaging. Bioconjugate Chemistry. 2014; 25: 796-801.

132. Roberts S, Seeger M, Jiang Y, Mishra A, Sigmund F, Stelzl A, et al. Calcium Sensor for Photoacoustic Imaging. Journal of the American Chemical Society. 2017.

133. Wang J, Chen F, Arconada-Alvarez SJ, Hartanto J, Yap L-P, Park R, et al. A Nanoscale Tool for Photoacoustic-based Measurements of Clotting Time and Therapeutic Drug Monitoring of Heparin. Nano Letters. 2016; 16: 6265-71.

134. Wang J, Jeevarathinam AS, Humphries K, Jhunjhunwala A, Chen F, Hariri A, et al. A Mechanistic Investigation of Methylene Blue and Heparin Interactions and Their Photoacoustic Enhancement. Bioconjugate chemistry. 2018.

135. Raschke RA, Reilly BM, Guidry JR, Fontana JR, Srinivas S. The weight-based heparin dosing nomogram compared with a standard care nomogram: a randomized controlled trial. Annals of Internal Medicine. 1993; 119: 874-81.

136. Jeon M, Song W, Huynh E, Kim J, Kim J, Helfield BL, et al. Methylene blue microbubbles as a model dual-modality contrast agent for ultrasound and activatable photoacoustic imaging. Journal of biomedical optics. 2014; 19: 016005.

137. Ashkenazi S. Photoacoustic lifetime imaging of dissolved oxygen using methylene blue. Journal of Biomedical Optics. 2010; 15: 040501.

138. Song KH, Stein EW, Margenthaler JA, Wang LV. Noninvasive photoacoustic identification of sentinel lymph nodes containing methylene blue in vivo in a rat model. Journal of biomedical optics. 2008; 13: 054033.

139. Morgounova E, Shao Q, Hackel BJ, Thomas DD, Ashkenazi S. Photoacoustic lifetime contrast between methylene blue monomers and self-quenched dimers as a model for dual-labeled activatable probes. Journal of biomedical optics. 2013; 18: 056004.

140. Wang J, Lin C-y, Moore C, Jhunjhunwala A, Jokerst JV. Switchable Photoacoustic Intensity of Methylene Blue via Sodium Dodecyl Sulfate Micellization. Langmuir. 2017.

141. Taruttis A, Morscher S, Burton NC, Razansky D, Ntziachristos V. Fast Multispectral Optoacoustic Tomography (MSOT) for Dynamic Imaging of Pharmacokinetics and Biodistribution in Multiple Organs. PLOS ONE. 2012; 7: e30491.

142. Razansky D, Distel M, Vinegoni C, Ma R, Perrimon N, Köster RW, et al. Multispectral opto-acoustic tomography of deep-seated fluorescent proteins in vivo. nature photonics. 2009; 3: 412.

143. Hannah A, Luke G, Wilson K, Homan K, Emelianov S. Indocyanine Green-Loaded Photoacoustic Nanodroplets: Dual Contrast Nanoconstructs for Enhanced Photoacoustic and Ultrasound Imaging. ACS Nano. 2014; 8: 250-9.

144. Hong G, Antaris AL, Dai H. Near-infrared fluorophores for biomedical imaging. Nature Biomedical Engineering. 2017; 1: 0010.

145. Pappone C, Rosanio S, Oreto G, Tocchi M, Gugliotta F, Vicedomini G, et al. Circumferential radiofrequency ablation of pulmonary vein ostia. Circulation. 2000; 102: 2619-28.

146. Pacella CM, Bizzarri G, Spiezia S, Bianchini A, Guglielmi R, Crescenzi A, et al. Thyroid tissue: US-guided percutaneous laser thermal ablation. Radiology. 2004; 232: 272-80.

147. Young JK, Figueroa ER, Drezek RA. Tunable nanostructures as photothermal theranostic agents. Annals of biomedical engineering. 2012; 40: 438-59.

148. Huang X, El-Sayed IH, Qian W, El-Sayed MA. Cancer cell imaging and photothermal therapy in the near-infrared region by using gold nanorods. Journal of the American Chemical Society. 2006; 128: 2115-20.

149. Shashkov EV, Everts M, Galanzha EI, Zharov VP. Quantum dots as multimodal photoacoustic and photothermal contrast agents. Nano letters. 2008; 8: 3953-8.

150. Yang K, Zhang S, Zhang G, Sun X, Lee S-T, Liu Z. Graphene in mice: ultrahigh in vivo tumor uptake and efficient photothermal therapy. Nano letters. 2010; 10: 3318-23.

151. Ke H, Wang J, Dai Z, Jin Y, Qu E, Xing Z, et al. Gold-Nanoshelled Microcapsules: A Theranostic Agent for Ultrasound Contrast Imaging and Photothermal Therapy. Angewandte Chemie. 2011; 123: 3073-7.

152. Huang P, Lin J, Li W, Rong P, Wang Z, Wang S, et al. Biodegradable gold nanovesicles with an ultrastrong plasmonic coupling effect for photoacoustic imaging and photothermal therapy. Angewandte Chemie. 2013; 125: 14208-14.

153. Lin L-S, Cong Z-X, Cao J-B, Ke K-M, Peng Q-L, Gao J, et al. Multifunctional Fe3O4@Polydopamine Core-Shell Nanocomposites for Intracellular mRNA Detection and Imaging-Guided Photothermal Therapy. ACS Nano. 2014; 8: 3876-83.

154. Lovell JF, Jin CS, Huynh E, MacDonald TD, Cao W, Zheng G. Enzymatic Regioselection for the Synthesis and Biodegradation of Porphysome Nanovesicles. Angewandte Chemie International Edition. 2012; 51: 2429-33.

155. Cheng L, Liu J, Gu X, Gong H, Shi X, Liu T, et al. PEGylated WS2 Nanosheets as a Multifunctional Theranostic Agent for in vivo Dual-Modal CT/Photoacoustic Imaging Guided Photothermal Therapy. Advanced Materials. 2014; 26: 1886-93.

156. Chen Y-S, Yoon SJ, Frey W, Dockery M, Emelianov S. Dynamic contrast-enhanced photoacoustic imaging using photothermal stimuli-responsive composite nanomodulators. Nature communications. 2017; 8: 15782.

157. Lightdale CJ, Heier SK, Marcon NE, McCaughan JS, Gerdes H, Overholt BF, et al. Photodynamic therapy with porfimer sodium versus thermal ablation therapy with Nd: YAG laser for palliation of esophageal cancer: a multicenter randomized trial. Gastrointestinal endoscopy. 1995; 42: 507-12.

158. Hongcharu W, Taylor CR, Aghassi D, Suthamjariya K, Anderson RR, Chang Y. Topical ALA-photodynamic therapy for the treatment of acne vulgaris. Journal of Investigative Dermatology. 2000; 115: 183-92.

159. Kharkwal GB, Sharma SK, Huang YY, Dai T, Hamblin MR. Photodynamic therapy for infections: clinical applications. Lasers in surgery and medicine. 2011; 43: 755-67.

160. Bressler N. Photodynamic therapy of subfoveal choroidal neovascularization in age-related macular degeneration with verteporfin: two-year results of 2 randomized clinical trials-tap report 2. Archives of ophthalmology (Chicago, Ill: 1960). 2001; 119: 198-207.

161. Agostinis P, Berg K, Cengel KA, Foster TH, Girotti AW, Gollnick SO, et al. Photodynamic therapy of cancer: an update. CA: a cancer journal for clinicians. 2011; 61: 250-81.

162. Ho CJH, Balasundaram G, Driessen W, McLaren R, Wong CL, Dinish U, et al. Multifunctional photosensitizer-based contrast agents for photoacoustic imaging. Scientific reports. 2014; 4.

163. Idris NM, Gnanasammandhan MK, Zhang J, Ho PC, Mahendran R, Zhang Y. In vivo photodynamic therapy using upconversion nanoparticles as remote-controlled nanotransducers. Nature medicine. 2012; 18: 1580-5.

164. Shao P, Chapman DW, Moore RB, Zemp RJ. Monitoring photodynamic therapy with photoacoustic microscopy. SPIE; 2015: 6.

165. Srivatsan A, Jenkins SV, Jeon M, Wu Z, Kim C, Chen J, et al. Gold nanocage-photosensitizer conjugates for dual-modal image-guided enhanced photodynamic therapy. Theranostics. 2014; 4: 163.

166. Lin J, Wang S, Huang P, Wang Z, Chen S, Niu G, et al. Photosensitizer-loaded gold vesicles with strong plasmonic coupling effect for imaging-guided photothermal/photodynamic therapy. ACS nano. 2013; 7: 5320-9.

167. Guo W, Qiu Z, Guo C, Ding D, Li T, Wang F, et al. Multifunctional Theranostic Agent of Cu2(OH)PO4 Quantum Dots for Photoacoustic Image-Guided Photothermal/Photodynamic Combination Cancer Therapy. ACS Applied Materials & Interfaces. 2017; 9: 9348-58.

168. Clift MJD, Stone V. Quantum dots: an insight and perspective of their biological interaction and how this relates to their relevance for clinical use. Theranostics. 2012; 2: 668-80.

169. Laufer J, Johnson P, Zhang E, Treeby B, Cox B, Pedley B, et al. In vivo preclinical photoacoustic imaging of tumor vasculature development and therapy. Journal of biomedical optics. 2012; 17: 0560161-8.

170. Bohndiek SE, Sasportas LS, Machtaler S, Jokerst JV, Hori S, Gambhir SS. Photoacoustic Tomography Detects Early Vessel Regression and Normalization During Ovarian Tumor Response to the Antiangiogenic Therapy Trebananib. J Nucl Med. 2015; 56: 1942-7.

171. Zhang J, Zhen X, Upputuri PK, Pramanik M, Chen P, Pu K. Activatable Photoacoustic Nanoprobes for In Vivo Ratiometric Imaging of Peroxynitrite. Advanced Materials. 2017; 29: 1604764.

172. Kim T, Zhang Q, Li J, Zhang L, Jokerst JV. A Gold/Silver Hybrid Nanoparticle for Treatment and Photoacoustic Imaging of Bacterial Infection. ACS Nano. 2018; 12: 5615-25.

173. Ng KK, Shakiba M, Huynh E, Weersink RA, Roxin Á, Wilson BC, et al. Stimuli-Responsive Photoacoustic Nanoswitch for in Vivo Sensing Applications. ACS Nano. 2014; 8: 8363-73.

174. Dragulescu-Andrasi A, Kothapalli S-R, Tikhomirov GA, Rao J, Gambhir SS. Activatable Oligomerizable Imaging Agents for Photoacoustic Imaging of Furin-Like Activity in Living Subjects. Journal of the American Chemical Society. 2013; 135: 11015-22.

175. Luis Dean-Ben X, Razansky D. Adding fifth dimension to optoacoustic imaging: volumetric time-resolved spectrally enriched tomography. Light Sci Appl. 2014; 3: e137.

176. Halliwell B. Reactive oxygen species in living systems: source, biochemistry, and role in human disease. The American journal of medicine. 1991; 91: S14-S22.

177. Alfadda AA, Sallam RM. Reactive Oxygen Species in Health and Disease. Journal of Biomedicine and Biotechnology. 2012; 2012: 14.

178. Brieger K, Schiavone S, Miller Jr FJ, Krause K-H. Reactive oxygen species: from health to disease. Swiss medical weekly. 2012; 142: w13659.

179. Görlach A, Dimova EY, Petry A, Martínez-Ruiz A, Hernansanz-Agustín P, Rolo AP, et al. Reactive oxygen species, nutrition, hypoxia and diseases: Problems solved? Redox Biology. 2015; 6: 372-85.

180. Pu K, Shuhendler AJ, Jokerst JV, Mei J, Gambhir SS, Bao Z, et al. Semiconducting polymer nanoparticles as photoacoustic molecular imaging probes in living mice. Nat Nano. 2014; 9: 233-9.

181. Pacher P, Beckman JS, Liaudet L. Nitric oxide and peroxynitrite in health and disease. Physiological reviews. 2007; 87: 315-424.

182. Yoon Y, Lee PJ, Kurilova S, Cho W. In situ quantitative imaging of cellular lipids using molecular sensors. Nat Chem. 2011; 3: 868-74.

183. Kullo IJ, Trejo-Gutierrez JF, Lopez-Jimenez F, Thomas RJ, Allison TG, Mulvagh SL, et al. A Perspective on the New American College of Cardiology/American Heart Association Guidelines for Cardiovascular Risk Assessment. Mayo Clinic Proceedings. 89: 1244-56.

184. Beard PC, Mills T. Characterization of post mortem arterial tissue using time-resolved photoacoustic spectroscopy at 436, 461 and 532 nm. Physics in medicine and biology. 1997; 42: 177.

185. Allen TJ, Beard PC. Photoacoustic characterisation of vascular tissue at NIR wavelengths. 2009: 71770A-A-9.

186. Abran M, Cloutier G, Cardinal M-HR, Chayer B, Tardif J-C, Lesage F. Development of a photoacoustic, ultrasound and fluorescence imaging catheter for the study of atherosclerotic plaque. IEEE transactions on biomedical circuits and systems. 2014; 8: 696-703.

187. Sangha GS, Phillips EH, Goergen CJ. In vivo photoacoustic lipid imaging in mice using the second near-infrared window. Biomedical optics express. 2017; 8: 736-42.

188. Wilson RH, Nadeau KP, Jaworski FB, Tromberg BJ, Durkin AJ. Review of short-wave infrared spectroscopy and imaging methods for biological tissue characterization. Journal of Biomedical Optics. 2015; 20: 030901.

189. Wang P, Ma T, Slipchenko MN, Liang S, Hui J, Shung KK, et al. High-speed intravascular photoacoustic imaging of lipid-laden atherosclerotic plaque enabled by a 2-kHz barium nitrite raman laser. Scientific reports. 2014; 4: 6889.

190. Chen YS, Frey W, Walker C, Aglyamov S, Emelianov S. Sensitivity enhanced nanothermal sensors for photoacoustic temperature mapping. Journal of biophotonics. 2013; 6: 534-42.

191. Larina IV, Larin KV, Esenaliev RO. Real-time optoacoustic monitoring of temperature in tissues. Journal of Physics D: Applied Physics. 2005; 38: 2633.

192. Ke H, Tai S, Wang LV. Photoacoustic thermography of tissue. Journal of biomedical optics. 2014; 19: 026003.

193. Wang S-H, Wei C-W, Jee S-H, Li P-C. Photoacoustic temperature measurements for monitoring of thermal therapy. Photons Plus Ultrasound: Imaging and Sensing 2009: International Society for Optics and Photonics; 2009: 71771S.

194. Zhou Y, Tang E, Luo J, Yao J. Deep-tissue temperature mapping by multi-illumination photoacoustic tomography aided by a diffusion optical model: a numerical study. SPIE; 2018: 10.

195. Liu W, Lan B, Hu L, Chen R, Zhou Q, Yao J. Photoacoustic thermal flowmetry with a single light source. SPIE; 2017: 6.

196. Gillies R, Raghunand N, Garcia-Martin M, Gatenby R. pH imaging: A review of pH measurement methods and applications in cancers; 2004.

197. Han J, Burgess K. Fluorescent Indicators for Intracellular pH. Chemical Reviews. 2010; 110: 2709-28.

198. Miao Q, Lyu Y, Ding D, Pu K. Semiconducting Oligomer Nanoparticles as an Activatable Photoacoustic Probe with Amplified Brightness for In Vivo Imaging of pH. Advanced Materials. 2016; 28: 3662-8.

199. Huang P, Gao Y, Lin J, Hu H, Liao H-S, Yan X, et al. Tumor-Specific Formation of Enzyme-Instructed Supramolecular Self-Assemblies as Cancer Theranostics. ACS Nano. 2015; 9: 9517-27.

200. Mu J, Lin J, Huang P, Chen X. Development of endogenous enzyme-responsive nanomaterials for theranostics. Chemical Society Reviews. 2018.

201. Xu Y, Wang LV. Effects of acoustic heterogeneity in breast thermoacoustic tomography. IEEE transactions on ultrasonics, ferroelectrics, and frequency control. 2003; 50: 1134-46.

202. Hariri A, Fatima A, Mohammadian N, Mahmoodkalayeh S, Ansari MA, Bely N, et al. Development of low-cost photoacoustic imaging systems using very low-energy pulsed laser diodes. Journal of biomedical optics. 2017; 22: 075001.

203. Hariri A, Lemaster J, Wang J, Jeevarathinam AS, Chao DL, Jokerst JV. The characterization of an economic and portable LED-based photoacoustic imaging system to facilitate molecular imaging. Photoacoustics. 2018; 9: 10-20.

204. Zhu Y, Xu G, Yuan J, Jo J, Gandikota G, Demirci H, et al. Light emitting diodes based photoacoustic imaging and potential clinical applications. Scientific reports. 2018; 8: 9885.

205. Antaris AL, Chen H, Diao S, Ma Z, Zhang Z, Zhu S, et al. A high quantum yield molecule-protein complex fluorophore for near-infrared II imaging. Nature communications. 2017; 8: 15269.

206. Zhu S, Yang Q, Antaris AL, Yue J, Ma Z, Wang H, et al. Molecular imaging of biological systems with a clickable dye in the broad 800-to 1,700-nm near-infrared window. Proceedings of the National Academy of Sciences. 2017; 114: 962-7.

207. Finlay MC, Mosse CA, Colchester RJ, Noimark S, Zhang EZ, Ourselin S, et al. Through-needle all-optical ultrasound imaging in vivo: a preclinical swine study. Light: Science &Amp; Applications. 2017; 6: e17103.

208. Xi L, Jiang H. Integrated photoacoustic and diffuse optical tomography system for imaging of human finger joints in vivo. Journal of Biophotonics. 2016; 9: 213-7.

209. Lin CY, Chen F, Hariri A, Chen CJ, Wilder-Smith P, Takesh T, et al. Photoacoustic Imaging for Noninvasive Periodontal Probing Depth Measurements. Journal of Dental Research. 2017: 0022034517729820.

210. Moore C, Bai Y, Hariri A, Sanchez JB, Lin C-Y, Koka S, et al. Photoacoustic imaging for monitoring periodontal health: A first human study. Photoacoustics. 2018; 12: 67-74.

211. Aliroteh M, Scott G, Arbabian A. Frequency-modulated magneto-acoustic detection and imaging. Electronics letters. 2014; 50: 790-2.

212. Mehrmohammadi M, Oh J, Aglyamov SR, Karpiouk AB, Emelianov SY. Pulsed magneto-acoustic imaging. Engineering in Medicine and Biology Society, 2009 EMBC 2009 Annual International Conference of the IEEE: IEEE; 2009: 4771-4.